Evolution of a proto-neutron star with a nuclear many-body equation of state: Neutrino luminosity and gravitational wave frequencies

Giovanni Camelio,[1,2,*] Alessandro Lovato,[3] Leonardo Gualtieri,[1,†] Omar Benhar,[1] José A. Pons,[4,‡] and Valeria Ferrari[1,§]

[1]*Dipartimento di Fisica, "Sapienza" Università di Roma & Sezione INFN Roma1, P.A. Moro 5, 00185 Roma, Italy*
[2]*Astronomy and Oskar Klein Centre, Stockholm University, AlbaNova, SE-10691 Stockholm, Sweden*
[3]*Physics Division, Argonne National Laboratory, Argonne, Illinois 60439, USA*
[4]*Departament de Física Aplicada, Universitat d'Alacant, Apartat de Correus 99, 03080 Alacant, Spain*

(Received 11 April 2017; published 30 August 2017)

In a core-collapse supernova, a huge amount of energy is released in the Kelvin-Helmholtz phase subsequent to the explosion, when the proto-neutron star cools and deleptonizes as it loses neutrinos. Most of this energy is emitted through neutrinos, but a fraction of it can be released through gravitational waves. We model the evolution of a proto-neutron star in the Kelvin-Helmholtz phase using a general relativistic numerical code, and a recently proposed finite temperature, many-body equation of state; from this we consistently compute the diffusion coefficients driving the evolution. To include the many-body equation of state, we develop a new fitting formula for the high density baryon free energy at finite temperature and intermediate proton fraction. We estimate the emitted neutrino signal, assessing its detectability by present terrestrial detectors, and we determine the frequencies and damping times of the quasinormal modes which would characterize the gravitational wave signal emitted in this stage.

DOI: 10.1103/PhysRevD.96.043015

I. INTRODUCTION

When a star with mass greater than about 8 $M_\odot$ exhausts its fuel, the electron Fermi pressure cannot prevent the collapse of the stellar core. In a few milliseconds, the density of the collapsing core reaches the nucleon density, the pressure due to the nucleon Fermi degeneracy and nuclear interaction sets in, the collapse halts, and a shock wave is generated as the exterior core layers bounce off the core. Then, on a longer time scale the stellar core keeps on contracting as it cools and deleptonizes, while the shock wave proceeds through the stellar envelope. This part of the evolution is known as the Kelvin-Helmholtz phase, and the contracting stellar core is called proto-neutron star (PNS). This phase lasts for tens of seconds, during which the PNS matter is opaque to neutrinos. It has been shown that, after about 200 ms from the core bounce, the PNS evolution can be modeled as a sequence of quasistationary configurations, where neutrino diffusion determines the thermal and composition evolution of the hot remnant [1–3]. When the PNS has radiated about 10^{53} erg $\simeq 0.1\ M_\odot$ by neutrinos, the temperature is low enough for the matter to become neutrino transparent, and a neutron star is born.

The observation of a nearby supernova in the Large Magellanic Clouds in 1987, and the simultaneous detection of 19 neutrinos [4,5] have been milestones for both astrophysics and particle physics. Since then, impressive progress has been made in the modeling of supernova (SN) explosions. Numerical codes have been developed to study the highly dynamical process of core collapse and core bounce. From the earlier 1D simulations, multidimensionality has been extended to one + two and one + three, while including more and more complex physical inputs (for a recent review, see e.g. [6]). The effort in modeling the subsequent PNS phase has been comparatively smaller, even though a considerable amount of energy is emitted in this phase.

Because of its much longer time scale, for many years, the complex core-collapse numerical codes have not been able to describe the PNS phase. Only recently core-collapse codes have been able to describe the PNS phase [7,8], mainly with the aim of studying the nucleosynthesis processes due to the neutrino wind.

The quasistationary evolution of a PNS was first studied in [1]. After this first, seminal work in the past years a number of papers have addressed several related issues, as for instance the sensitivity of the PNS evolution and of the related neutrino signal to the nuclear equation of state (EOS) [2,3,9], the possible delayed formation of black holes [3,9], convective effects in presence of accretion [9–13], and nucleosynthesis due to the neutrino wind [14].

In addition, the frequencies at which a gravitational wave (GW) signal would be emitted by an oscillating PNS have been computed in [15,16], using quasiequilibrium configurations obtained from the evolutionary code of Pons

*giovanni.camelio@astro.su.se
†leonardo.gualtieri@roma1.infn.it
‡jose.pons@ua.es
§valeria.ferrari@roma1.infn.it

et al. [3], based on a mean-field EOS. In [17], a many-body EOS was employed, but the entropy and lepton fraction profiles were included "by hand" in order to mimic a time evolution similar to that found in [3]. The entropy and lepton fraction profiles were included in a similar way in [18], in order to mimic the profiles obtained, in the first second after bounce, by numerical core-collapse simulations. However, the EOSs they employed (such as that of Lattimer and Swesty [19]) are more appropriate to describe the core-collapse phase than the PNS evolution. We remark that, up to now, finite temperature, many-body nuclear dynamics have not been included in a consistent way (i.e., accounting for the modifications in the neutrino cross sections) in PNS evolution.

In this paper we describe the results of a new PNS evolutionary code and a formula that allows to fit a general nucleonic EOS at finite temperature, as the recently proposed many-body EOS of [20,21]. Using this code and three different EOSs (among which, the many-body EOS proposed in [20,21]), we study the PNS evolution during the Kelvin-Helmholtz phase. We estimate the neutrino luminosity, and compute the frequencies and damping times of the PNS quasinormal modes (QNMs), which characterize the emitted GW signal.

The work is organized as follows. In Sec. II we describe the nucleonic EOSs adopted in this paper and a new nucleonic fitting formula for the free energy. In Sec. III we describe how we compute the diffusion coefficient, and show how we effectively describe the baryon single-particle spectra by means of effective masses and single-particle potentials. In Sec. IV we show the results of our evolutionary code, and discuss how the relevant quantities, which describe the stellar structure and the neutrino luminosity, change in time. We also determine the neutrino signal in the Super-Kamiokande III detector for our models. In Sec. V we describe the computation of the QNM frequencies and damping times, and we discuss how the first QNMs change as the PNS evolve. We derive a relation between the frequencies of the fundamental mode and of the first pressure mode, and the mean stellar density. In Sec. VI we draw our conclusions. In Appendix A we provide the details of the fitting procedure of the nucleonic EOS; in Appendix B we discuss the convergence of our PNS code and justify some of the approximations made; in Appendix C we tabulate the frequencies and damping times of the QNMs of the stellar configurations we consider.

Unless otherwise stated, we set to unity the speed of light, the Boltzmann constant, and the gravitational constant $c = k_B = G = 1$. The "microscopic" masses, like the bare and effective masses of neutron and proton, are given in MeV. The "macroscopic" masses, that is, the PNS baryon and gravitational masses, are given in terms of the Sun mass $M_\odot$. We include the rest mass in the chemical potential and in the energy density.

II. THE EQUATION OF STATE

In this paper we compare three different finite-temperature nucleonic EOSs: a mean-field EOS, GM3 [22,23]; a nuclear many-body EOS, CBF-EI, obtained using the correlated basis function theory [20,21]; and a model based on the extrapolation from the measured nuclear properties, LS-bulk [19]. In all EOSs the leptonic part consists of a Fermi gas of noninteracting electrons, positrons and neutrinos of all flavours, where neutrinos are treated as massless particles. The baryonic part consists of an interacting Fermi gas of protons and neutrons. We neglect the Coulomb force between protons (which is screened by the electrons), we assume charge-independent nuclear interactions, and the proton and neutron bare masses are set equal, $m_p \equiv m_n$. Since we are interested in the evolution of a proto-neutron star, pasta phases or a solid crust are not included in our model. We have checked *a posteriori* that this approximation is justified, since the PNS temperature is always above the critical temperature for the formation of alpha particles, with the exception of the end of the cooling phase, when this approximation is no longer accurate in the region near the stellar surface (see Appendix B 3).

In the GM3 EOS, baryons—described by quantum fields—interact through the exchange of bosons (the σ, ω and ρ mesons). The resulting equations of motion are solved in the mean-field approximation, which amounts to treating mesons as classical fields. The LS-bulk EOS, specifically designed to be easily implemented in stellar collapse simulations, is based on a dynamical model constrained by nuclear phenomenology, and corresponds to the bulk part of the Lattimer and Swesty [19] EOS. The CBF-EI EOS (that stands for "correlated basis functions—effective interaction") has been obtained within nonrelativistic many-body theory, using a realistic nuclear Hamiltonian, which includes the Argonne v_6' and the Urbana IX nuclear potentials. The formalism of correlated basis functions and the cluster expansion technique have been used to devise an effective nucleon-nucleon potential, which includes the effects of both two- and three-nucleon forces, as well as nuclear correlations. This effective potential is well behaved and allows to describe both cold and hot matter, at arbitrary proton fraction at the Hartree-Fock level.

It is easy and fast to compute the GM3 and LS-bulk EOSs during the simulation. Conversely, due to their heavy computational cost, this procedure cannot be adopted for many-body EOSs (like CBF-EI). Therefore, one should resort either to an interpolation, or to a fit. Since we are studying the evolution of a PNS, we would need thermodynamical consistency and continuity of the second order derivatives of the free energy [24]. It is difficult to interpolate a table in a thermodynamically consistent way, because in a PNS the EOS is characterized by three independent variables (see below). Therefore, to describe

the baryon interaction we will find, and use, a fitting formula.

A. Thermodynamical relations

The first law of thermodynamics can be written in terms of an infinitesimal variation of f, the free energy per baryon, as

$$\mathrm{d}f = -s\mathrm{d}T + \frac{P}{n_\mathrm{B}^2}\mathrm{d}n_\mathrm{B} + \sum_i \mu_i \mathrm{d}Y_i, \tag{1}$$

with

$$P = n_\mathrm{B}^2 \left.\frac{\partial f}{\partial n_\mathrm{B}}\right|_{T,\{Y_i\}}, \tag{2}$$

$$s = -\left.\frac{\partial f}{\partial T}\right|_{n_\mathrm{B},\{Y_i\}}, \tag{3}$$

$$\mu_i = \left.\frac{\partial f}{\partial Y_i}\right|_{T,n_\mathrm{B},\{Y_{j\neq i}\}}, \tag{4}$$

where s is the entropy per baryon, P the pressure, T the temperature, n_B the baryon number density, μ_i and Y_i are the chemical potential of particle i and its particle fraction (i.e., the number of particles i per baryon) respectively. Note that $f \equiv e - Ts$, e being the energy per baryon. In the following we will also use the energy density $\epsilon \equiv e n_\mathrm{B}$. We remark that we include the rest mass in the energy and in the free energy, and therefore the chemical potentials *include the rest mass*.

Since the number fractions $\{Y_i\}$ are not independent variables, one should consider the equation

$$\mu_i = \left.\frac{\partial (n_\mathrm{B} f)}{\partial n_i}\right|_{T,\{n_{j\neq i}\}}, \tag{5}$$

rather than Eq. (4). If only neutrons and protons are present, Eq. (5) gives

$$\mu_p = f_\mathrm{B} + \frac{P_\mathrm{B}}{n_\mathrm{B}} + (1 - Y_p)\left.\frac{\partial f_\mathrm{B}}{\partial Y_p}\right|_{T,n_\mathrm{B}}, \tag{6}$$

$$\mu_n = f_\mathrm{B} + \frac{P_\mathrm{B}}{n_\mathrm{B}} - Y_p \left.\frac{\partial f_\mathrm{B}}{\partial Y_p}\right|_{T,n_\mathrm{B}}, \tag{7}$$

where the subscript B means that we are considering only the baryon part of the EOS.

B. Baryon free energy fitting formula

In this section we shall discuss a fitting formula for the interacting part of the baryon free energy; we remark that all thermodynamical quantities can be obtained in terms of partial derivatives of the free energy. We shall not consider here the kinetic part, which is the standard fermionic free energy (see Sec. II C), and the leptonic free energy, which will also be discussed in Sec. II C. In the following, the superscripts I and K refer to the interacting and kinetic parts of the thermodynamical quantities, respectively:

$$f_\mathrm{B}(Y_p, T, n_\mathrm{B}) = f_\mathrm{B}^K(Y_p, T, n_\mathrm{B}) + f_\mathrm{B}^I(Y_p, T, n_\mathrm{B}). \tag{8}$$

To begin with, we discuss the dependency of f_B^I on the proton fraction Y_p. In a zero-temperature EOS, the baryon free energy coincides with the baryon energy e_B. Its dependence on Y_p is well approximated [25] by

$$\begin{aligned} e_\mathrm{B}^I(Y_p, T=0) &= e_\mathrm{SNM}^I + (1-2Y_p)^2(e_\mathrm{PNM}^I - e_\mathrm{SNM}^I) \\ &= 4Y_p(1-Y_p)e_\mathrm{SNM}^I + (1-2Y_p)^2 e_\mathrm{PNM}^I, \end{aligned} \tag{9}$$

where $e_\mathrm{SNM}^I = e_\mathrm{B}^I(Y_p = 1/2, T=0)$ and $e_\mathrm{PNM}^I = e_\mathrm{B}^I(Y_p = 0, T=0)$ are the baryon interacting energies of the symmetric (SNM) and pure neutron matter (PNM), respectively, at zero temperature.

Following [26], we assume that finite-temperature effects do not modify the functional dependency of f_B^I on the proton fraction, i.e.,

$$\begin{aligned} f_\mathrm{B}^I(Y_p, T, n_\mathrm{B}) &= 4Y_p(1-Y_p) f_\mathrm{SNM}^I(T, n_\mathrm{B}) \\ &\quad + (1-2Y_p)^2 f_\mathrm{PNM}^I(T, n_\mathrm{B}), \end{aligned} \tag{10}$$

where f_SNM^I and f_PNM^I are the baryon interacting free energies per baryon for symmetric and pure neutron matter. We verify the accuracy of this assumption *a posteriori*: for *given values* of temperature and baryon density, the difference between the interacting baryon free energy and the quadratic fit in Y_p is $\lesssim$0.02 MeV for the GM3 EOS and $\lesssim$0.05 MeV for the CBF-EI EOS, to be compared with an interacting baryon free energy on the order of $\sim$10 MeV.

We now discuss the dependency of the interacting part of the baryon free energy on the temperature and on the baryon number density, i.e., the fitting formulas of symmetric and pure neutron matter, $f_\mathrm{SNM}^I(T, n_\mathrm{B})$ and $f_\mathrm{PNM}^I(T, n_\mathrm{B})$, appearing in Eq. (10). In the literature, there is no generally accepted fitting formula for these functions [19,26–29]. In order to perform our evolutionary numerical simulations, we need a fitting formula which is accurate in a wide density range, extending from $n_\mathrm{B} \lesssim 0.5$ fm^{-3} to $n_\mathrm{B} \gtrsim 0.001$ fm^{-3} relevant for the core and the crust of the star, respectively. Therefore, we cannot use the fitting formula of [26], which is only accurate for large densities. Moreover, we need a free energy with continuous second-order derivatives. Finally, the following constraints have to be fulfilled: (i) $s \to 0$ as $T \to 0$; (ii) in the low density limit the EOS must tend to that of a free gas, i.e., $f_\mathrm{B}^I \to 0$,

$s_{\rm B}^I \to 0$, and $P_{\rm B}^I \to 0$, as $n_{\rm B} \to 0$. Under these conditions, in the range of temperatures and densities considered (see Appendix A), we find that a good trade-off between number of parameters and precision of the fit is given by the following polynomial fitting formula:

$$f_j^I(n_{\rm B}, T) = a_{1,j} n_{\rm B} + a_{2,j} n_{\rm B}^2 + a_{3,j} n_{\rm B}^3 + a_{4,j} n_{\rm B}^4 + n_{\rm B} T^2 (a_{5,j} + a_{6,j} T + a_{7,j} n_{\rm B} + a_{8,j} n_{\rm B} T), \tag{11}$$

where $j = \{\text{SNM}; \text{PNM}\}$. We have performed the fit (10), (11) for the EOSs GM3 and CBF-EI. The details of the fitting procedure, and the values of the coefficients $a_{n,i}$, for these two EOSs are given in Appendix A. For the LS-bulk EOS we have used the analytical expression given in [19],

$$f_{\rm B}^I = [a + 4bY_p(1 - Y_p)] n_{\rm B} + c n_{\rm B}^{\delta} - Y_p \Delta_m, \tag{12}$$

with

$$\begin{aligned} \delta &= 1.260, \\ a &= -711.0 \text{ MeV fm}^3, \\ b &= -107.1 \text{ MeV fm}^3, \\ c &= 934.6 \text{ MeV fm}^{3\delta}, \\ \Delta_m &= 0 \text{ MeV}. \end{aligned} \tag{13}$$

This choice of parameters corresponds to a binding energy BE $= -16$ MeV, a saturation density $n_s = 0.155$ fm^{-3}, an incompressibility at saturation $K_s = 220$ MeV, a symmetry energy parameter at saturation $S_v = 29.3$ MeV, and a vanishing neutron-proton mass difference Δ_m. As a comparison, the GM3 EOS has $n_s = 0.153$ fm^{-3}, BE $= -16.3$ MeV, $K_s = 240$ MeV, $S_v = 32.5$ MeV, and $\Delta_m = 0$ [23]; the CBF-EI EOS has $n_s = 0.16$ fm^{-3}, BE $\simeq -11$ MeV, $K_s = 180$ MeV, $S_v = 30$ MeV, and a vanishing *bare* neutron-proton mass difference (conversely, the proton and neutron effective masses are different and change with density, temperature and composition). In Fig. 1 we show the mass-radius diagram for cold neutron stars for the three EOSs. To generate them, we have computed the zero-temperature EOSs at beta equilibrium, considering both muons and electrons. The CBF-EI EOS has been linearly extrapolated in the logarithms of P, $n_{\rm B}$, and ϵ for densities higher than $n_{\rm B} = 0.48$ fm^{-3}, enforcing causality ($c_s \leq 1$). This is necessary to describe the central region of stars with a gravitational mass $M \gtrsim 1.64\ M_\odot$, corresponding to a baryonic mass $M_b \gtrsim 1.84\ M_\odot$. The maximum mass for GM3 and LS-bulk is $M_{\rm max} \simeq 2.02\ M_\odot$, while for CBF-EI we get $M_{\rm max} \simeq 2.34\ M_\odot$.

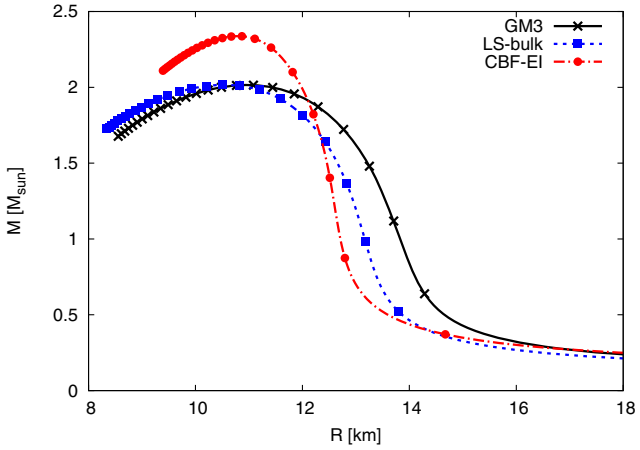

FIG. 1. $T = 0$ mass-radius diagrams for the three EOSs considered in this work.

C. Numerical implementation of the complete EOS

In Sec. II B we discussed the interacting part of the baryon EOS (composed of protons p and neutrons n). In addition, for the baryon kinetic part and for electrons and positrons we have adopted the EOS of free fermions given in [30,31], and for the three neutrino families the EOS of free massless fermions given in [19] [Eqs. (C1) and (C3)]. The thermodynamical quantities of the ith lepton are given in terms of the temperature and of the corresponding chemical potential μ_i.

During the PNS evolution other particles are expected to appear, like hyperons, muons, and tauons. Since we are mostly interested in comparing how mean-field and many-body EOSs affect the PNS evolution, we have focused on nucleons (many-body EOSs have been developed mainly for nucleons). Moreover, we do not include muons or tauons (as done also in [1,3]), since a consistent treatment of these particles would considerably increase the complexity of the transport scheme.

The PNS structure and the transport equations (Sec. IV A) suggest to use as independent variables the pressure P, the entropy per baryon s, and the electron lepton fraction $Y_L \equiv Y_e + Y_\nu$, where $Y_e \equiv Y_{e^-} - Y_{e^+}$ and $Y_\nu = Y_{\nu_e} - Y_{\bar{\nu}_e}$. To determine the different thermodynamical quantities of the complete EOS in terms of these variables, we use a Newton-Raphson cycle, in which we exploit the fitting formula discussed in Sec. II B for the baryonic interacting quantities, along with the leptonic EOS mentioned above, and we assume charge neutrality $Y_e \equiv Y_{e^-} - Y_{e^+} = Y_p$, beta equilibrium

$$\mu_{\nu_e} = \mu_p - \mu_n + \mu_{e^-}, \tag{14}$$

and the requirement that muon and tau neutrinos are not trapped:

$$\mu_{\nu_\mu} = \mu_{\nu_\tau} = 0, \tag{15}$$

$$\mu_{\bar{\nu}_{\{e,\mu,\tau\}}} = -\mu_{\nu_{\{e,\mu,\tau\}}}. \quad (16)$$

It is easy to obtain the GM3 quantities by directly solving the corresponding mean-field equations. For this reason, we have used GM3 as a benchmark for the fitting procedure of the baryon free energy.

D. EOSs comparison

In this subsection we compare the features of the three EOSs, and the accuracy of our fit for the baryon free energy, by considering three cases: (i) $Y_L = 0.4$ and $s = 1$, (ii) $Y_\nu \equiv Y_{\nu_e} = 0$ and $s = 2$ (corresponding to the end of the deleptonization phase), and (iii) $Y_\nu \equiv Y_{\nu_e} = 0$ and $T = 5$ MeV (which is the condition in most of the star at the end of our simulations, i.e., toward the end of the cooling phase).

In Fig. 2 we compare the behavior of the EOS GM3 (continuous line), GM3-fit obtained using the fitting formula (crosses), LS-bulk (dashed line), and CBF-EI (dot-dashed line). We plot the pressure, the energy density, and the sound speed, c_s, as functions of the baryon number density, for cases (i)–(iii) discussed above. Fig. 2 clearly shows that GM3-fit reproduces the behavior of GM3 EOS.

As already noted by Pons *et al.* [3], the pressure and the energy density in the three cases have a similar dependence on the number density, since they mainly depend on the baryon interaction and degeneracy, rather than on temperature. At the saturation density n_s (whose exact value is slightly different for the three EOSs, but is in the range $n_s = 0.15$–0.16 fm^{-3}), the sound speed is slightly larger (lower) for the EOS with larger (lower) incompressibility parameter K_s. At high baryon density, the sound speed of the CBF-EI EOS is larger than that of the LS-bulk and GM3 EOSs: this is due to a well-known problem of the many-body EOSs, which violate causality at very high density. However, in the regime of interest for this paper, this unphysical behavior can safely be neglected.

In Fig. 3 we plot the temperature versus n_B for $Y_L = 0.4$ and $s = 1$, and $Y_\nu \equiv Y_{\nu_e} = 0$ and $s = 2$ (left and central panels) and the entropy per baryon for $Y_\nu \equiv Y_{\nu_e} = 0$ and $T = 5$ MeV (right panel). From the right panel we see that, at a fixed temperature, GM3 reaches a given value of the entropy for a baryon density lower than that of LS-bulk and higher than that of CBF-EI. This behavior may be traced back to the fact that particles in the GM3 EOS are less correlated than in the CBF-EI EOS, and more correlated than in the LS-bulk EOS. Therefore, the CBF-EI describes a "more ordered" nuclear matter than GM3 and the entropy is lower. The left and central panels of Fig. 3, where we plot the temperature for fixed values of the entropy, show that CBF-EI is hotter than GM3, which is hotter than LS-bulk. As in Fig. 2, the GM3-fit reproduces the behavior of GM3 EOS.

III. NEUTRINO DIFFUSION COEFFICIENTS

A. The equations

The diffusion coefficients D_2, D_3, D_4 employed in the PNS evolution (Sec. IV) are given in [3]:

$$D_2 = D_2^{\nu_e} + D_2^{\bar{\nu}_e}, \quad (17)$$

$$D_3 = D_3^{\nu_e} - D_3^{\bar{\nu}_e}, \quad (18)$$

$$D_4 = D_4^{\nu_e} + D_4^{\bar{\nu}_e} + 4D_4^{\nu_\mu}, \quad (19)$$

$$D_n^{\nu_i} = \int_0^\infty \mathrm{x}^n \lambda_{\mathrm{tot}}^{\nu_i}(\omega) f^{\nu_i}(\omega)(1 - f^{\nu_i}(\omega))dx, \quad (20)$$

$$\lambda_{\mathrm{tot}}^{\nu_i}(\omega) = \left(\sum\nolimits_{j\in\mathrm{reactions}} \frac{\sigma_j^{\nu_i}(\omega)}{V}\right)^{-1}, \quad (21)$$

where $f^{\nu_i}(\omega) = [1 + \exp((\omega - \mu_{\nu_i})/T)]^{-1}$ and $\lambda_{\mathrm{tot}}^{\nu_i}(\omega)$ are the distribution function[1] and the total mean-free path of a ν_i neutrino of energy ω, respectively, and $x = \omega/T$. The ν_i neutrino cross section of the jth reaction is denoted with $\sigma_j^{\nu_i}$. All quantities depend upon the temperature and the particle chemical potentials, which are determined by the underlying EOS.

To determine the $\sigma_j^{\nu_i}$ we adopt the mean-field approach of [32] [Eq. (82)] that accounts for in-medium effects, including the scattering of all neutrino types on electrons, protons, and neutrons, and the absorption of electron neutrinos and electron antineutrinos on neutrons and protons, respectively, with the corresponding inverse processes, i.e.,

$$\nu_i + n \rightleftharpoons \nu_i + n, \quad (22)$$

$$\nu_i + p \rightleftharpoons \nu_i + p, \quad (23)$$

$$\nu_i + e^- \rightleftharpoons \nu_i + e^-, \quad (24)$$

$$\nu_e + n \rightleftharpoons e^- + p, \quad (25)$$

$$\bar{\nu}_e + p \rightleftharpoons e^+ + n. \quad (26)$$

Furthermore, we assume that the cross sections of all non-electronic neutrinos coincide with those of muon neutrinos. We do not include nucleon-nucleon Bremsstrahlung [33].

B. Effective masses and single-particle potentials

Identifying single-particle properties in interacting systems involves nontrivial conceptual difficulties. However, due to translation invariance, in infinite matter

[1]Here we set $\hbar = 1$ and assume that integrals are normalized as in [3,32].

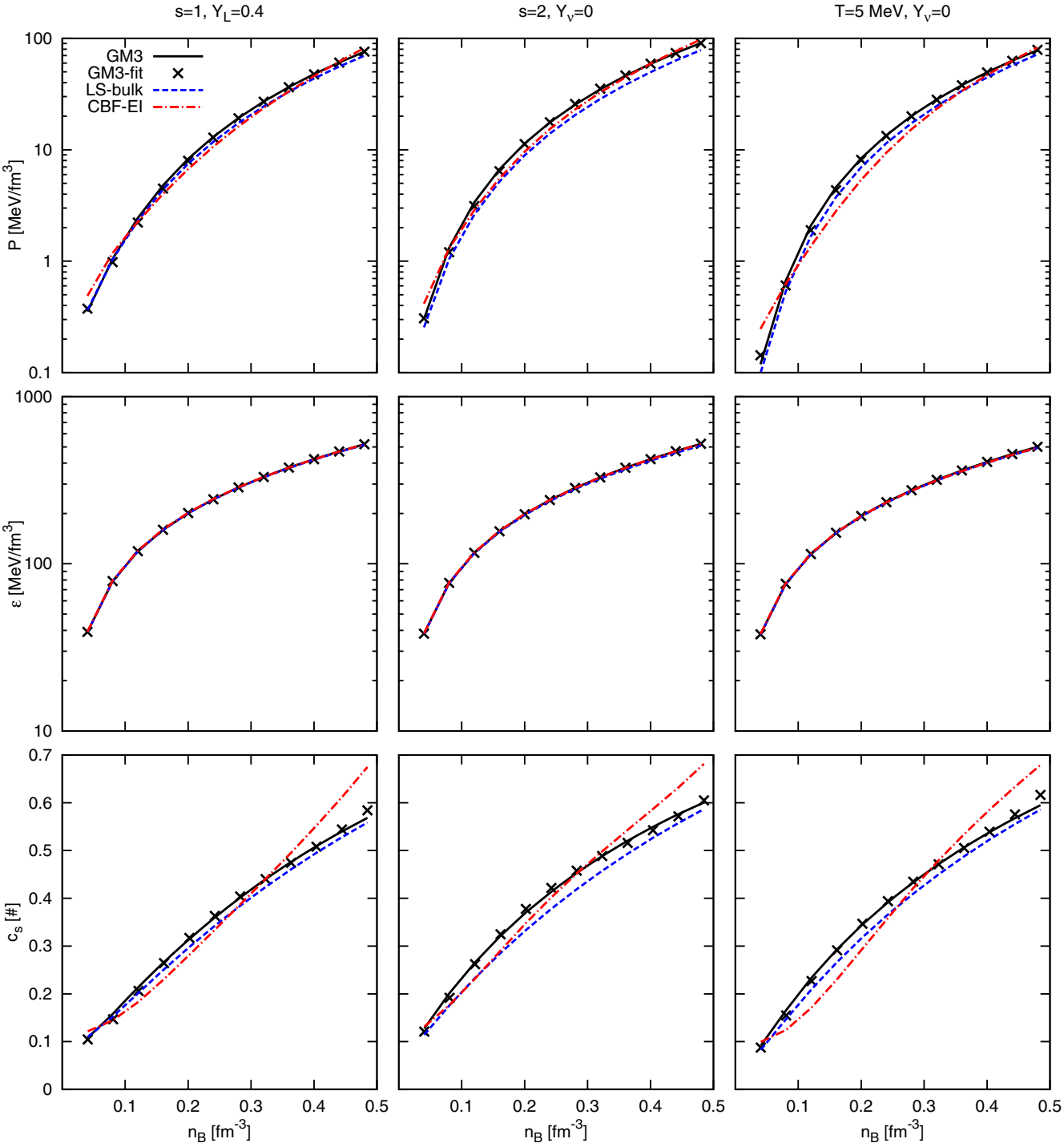

FIG. 2. The pressure (upper panels), the energy density (middle panels), and the speed of sound (bottom panels) are plotted versus the baryon number density for the EOSs considered in this paper, and for different values of selected parameters [cases (i)–(iii) described in Sec. II D]. The black solid line refers to the GM3 EOS determined by solving numerically the mean-field equations, the black crosses to the GM3 EOS determined through the fit and the procedure described in Sec. II C, the blue dashed line to the LS-bulk EOS, and the red dot-dashed line to the CBF-EI EOS.

single-particle states are labeled by the momentum $\mathbf{k}$, and the corresponding spectrum can be unambiguously identified. Within the nonrelativistic many-body theory, the spectrum of an interacting particle can be expressed as

$$\mathcal{E}(k) = m + \frac{k^2}{2m} + U(k), \tag{27}$$

where $k = |\mathbf{k}|$ and $U(k)$ is the momentum-dependent single-particle potential.

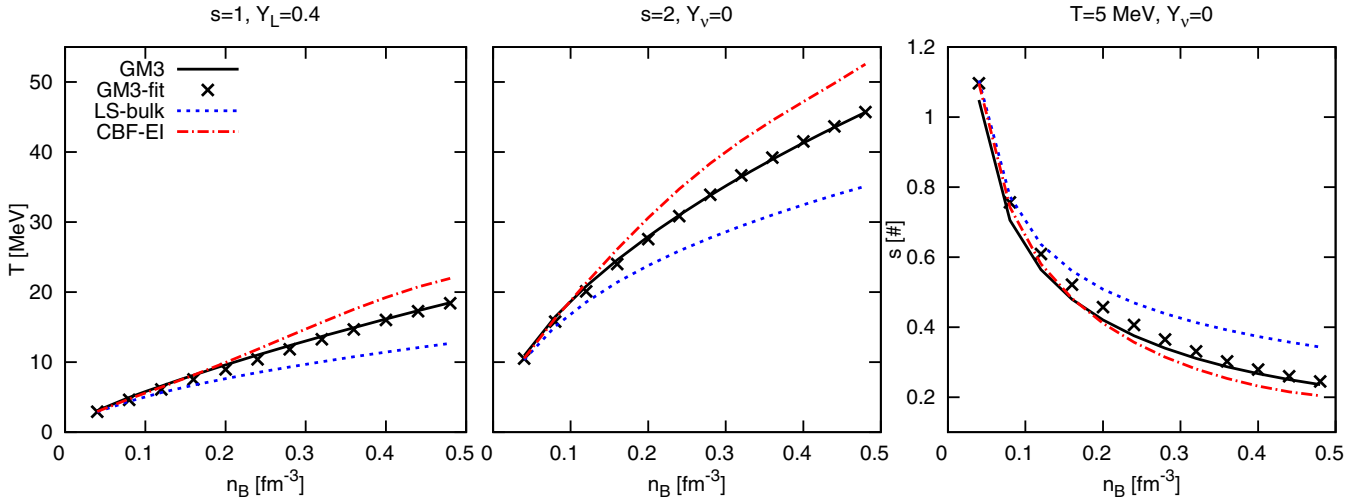

FIG. 3. Comparison among the three EOSs considered in this paper in the three cases described in Sec. II D. In the left and central plots we show the temperature and in the right plot we show the entropy per baryon. Colors and line styles are as in Fig. 2.

A widely used parametrization of $\mathcal{E}(k)$ is given in terms of momentum-independent effective mass m^* and single-particle potential U,

$$\mathcal{E}(k) \simeq m + \frac{k^2}{2m^*} + U. \tag{28}$$

Since the baryonic contributions to the mean-free paths and diffusion coefficients are mostly given by particles whose energies are close to the particle chemical potential, it is convenient to determine m^* and U from the behavior of the spectrum near the Fermi momentum,

$$\frac{1}{m_i^*} = \frac{1}{k_F}\frac{\partial \mathcal{E}_i}{\partial k}(k_F), \tag{29}$$

$$U_i = \mathcal{E}_i(k_F) - \frac{k_F^2}{2m_i^*} - m, \tag{30}$$

where $i = (\{p;n\}, Y_p, T, n_b)$.

Within the CBF-EI approach $\mathcal{E}(k)$ has been obtained at the Hartree-Fock level using the same effective potential employed for the calculation of the EOS. Therefore, the effective masses and the single-particle potentials are *consistent* with the EOS.

Equation (28) can be easily generalized to the relativistic case,

$$\mathcal{E}(k) = \sqrt{k^2 + m^{*2}} + U^*, \tag{31}$$

where we have introduced $U^* = U - m^* + m$. To treat the neutrino transport for the CBF-EI EOS consistently with that of the GM3 and LS-bulk EOSs, we compute the neutrino diffusion coefficients using Eq. (31) and the effective masses and single-particle potentials given in Eqs. (29) and (30).

We have verified that this approach reproduces, for the CBF-EI EOS, the correct baryon densities within ∼10% at saturation density.[2] This is important because the neutrino mean-free path [Eq. (21)] is an "intensive" quantity, and it depends on the baryon distribution functions. A discrepancy on the baryon densities n_B and the proton fraction Y_p would yield diffusion coefficients computed at wrong values of n_B and Y_p.

This applies also to the LS-bulk EOS, for which we have assumed that the baryon effective masses are equal to the neutron bare mass. To satisfy the aforementioned constraint (that the effective spectrum description yields the correct baryon density and proton fraction), we use a nonvanishing single-particle potential given by

$$U_i^* = \mu_i^I = \mu_i - \mu_i^K, \tag{32}$$

where $i = \{p;n\}$, μ is the chemical potential, and μ^I and μ^K are the interacting and free part of the particle chemical potential, respectively.

C. Numerical implementation

The neutrino diffusion coefficients are evaluated in the PNS evolution code by linear interpolation of a three-dimensional table, evenly spaced in Y_ν (the neutrino number fraction), T, and n_B. The table has been produced consistently with the underlying EOS, in the following way. We have first solved the EOS using the method described in Sec. II C, obtaining the proton fraction Y_p as a function of Y_ν, T, and n_B. The proton and neutron chemical potentials, effective masses, and the single-particle potentials for the GM3-fit and CBF-EI EOSs have been obtained by linear interpolation of a table evenly spaced in Y_p, T,

[2]The other baryon EOS quantities cannot be recovered from the baryonic spectrum as one should account also for the meson contributions. This is true also for the GM3 EOS, for which the description in terms of effective spectrum is exact.

and n_B. From these quantities, we determine the neutrino cross sections, and finally the neutrino diffusion coefficients [Eqs. (17)–(20)].

D. EOS comparison

In Fig. 4 we plot the neutrino diffusion coefficient D_2, the electron neutrino scattering mean-free path, and the

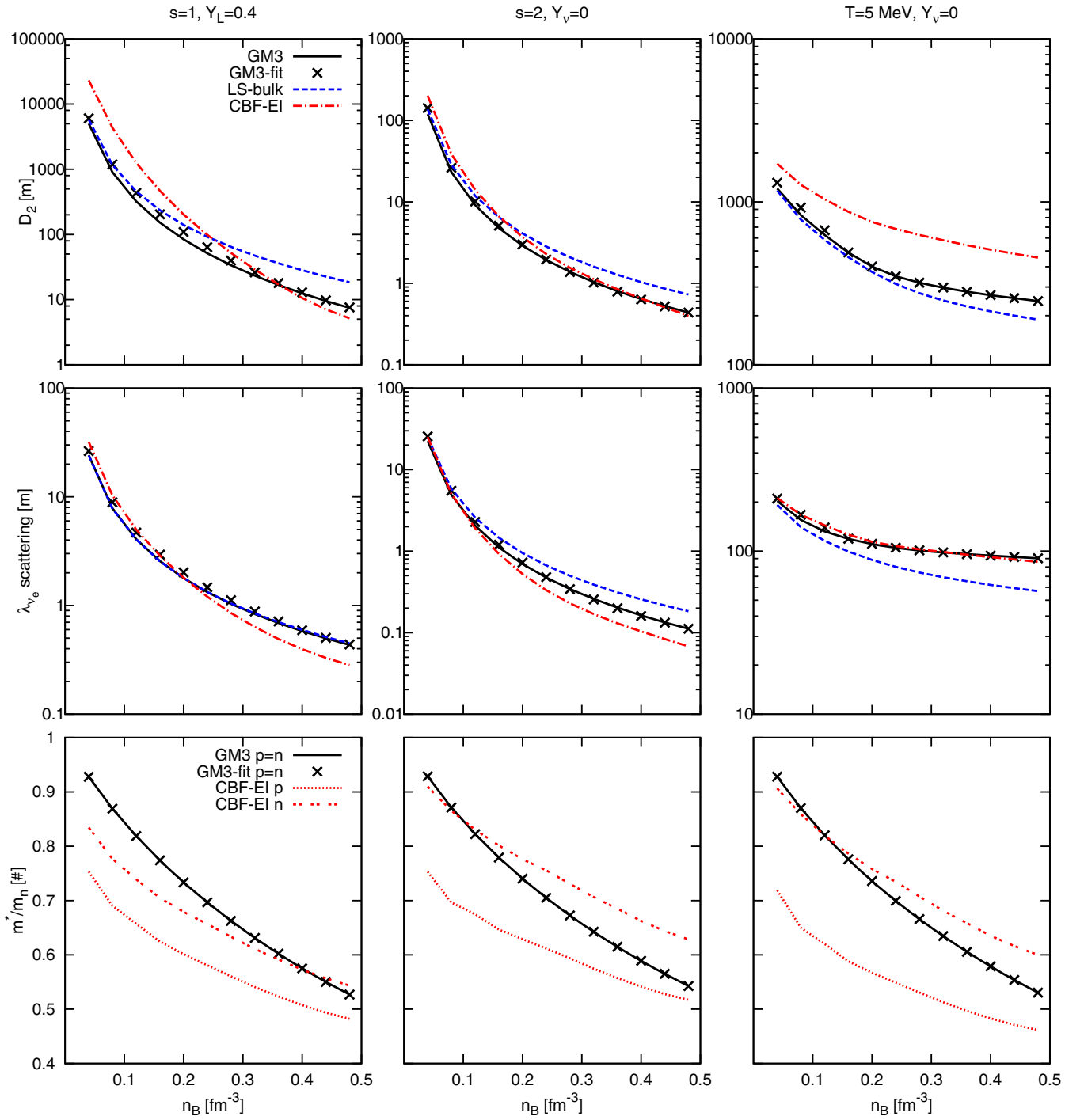

FIG. 4. Comparison between the diffusion coefficient D_2 (upper panel), the electron neutrino scattering mean-free paths [middle panel, the neutrino incoming energy is $E_{\nu_e} = \max(\mu_{\nu_e}, \pi T)$], and the baryon effective masses, m^*/m_n (lower panel) for the three EOSs considered in this paper in the three cases described in Sec. II D. For the GM3 EOS, the effective masses of proton and neutron are identical [22,23]. We do not show the LS-bulk EOS effective masses, since we have set them equal to the bare ones, $m^*_{\{p,n\}}/m_n = 1$. Colors and line styles are as in Fig. 2, apart for the line styles in the lower panel, where the CBF-EI proton (neutron) effective masses are dotted (double dashed).

baryon effective masses in the three cases described in Sec. II D. The incident neutrino energy which we have used to compute the neutrino mean-free path is $E_{\nu_e} = \max(\mu_{\nu_e}, \pi T)$. To understand the role of the interactions and of finite temperature in the neutrino diffusion, we consider their effects on the baryon distribution function. To fix ideas, let us consider the distribution function of a nonrelativistic fermion gas,

$$f(k) = \frac{1}{h^3}\left(1 + e^{\frac{k^2}{2m^*T} - \frac{\mu - U - m}{T}}\right)^{-1}. \tag{33}$$

If one decreases the temperature T or effective mass m^*, f approaches a Heaviside function, whereas increasing T or m^* it becomes smoother. Because of the Pauli principle, at lower temperatures T and effective masses m^* lower energy neutrinos can interact only with particles near the Fermi sphere, and therefore the mean-free paths and diffusion coefficients increase. Conversely, a greater temperature and effective mass imply that the mean-free paths and the diffusion coefficients are smaller. The scattering mean-free paths reflect the temperature dependence of the three EOSs: when the matter is hotter, the scattering is more effective (cf. lower plots of Fig. 3). At equal temperature, the interaction is more effective when the effective mass is greater. The behavior of the diffusion coefficient D_2 results from a complex interplay between scattering and absorption, for which the effective masses and single particle potentials play an important role. The comparison between the diffusion coefficient D_2 for the three EOSs suggests that towards the end of the cooling phase (in which the thermodynamical conditions are roughly similar to those in the right plots of Fig. 4), the CBF-EI star evolves faster than the other EOSs.

As in Figs. 2 and 3, GM3-fit (for which the baryon spectra effective parameters are determined by table interpolation, Sec. III C) reproduces the results of the GM3 EOS.

IV. PNS EVOLUTION

A. The equations

We developed a numerical code to model the PNS evolution. Our code is similar to that of Pons *et al.* [3]: it is energy averaged (the neutrino distribution function has been assumed Fermi-Dirac and in thermal equilibrium with matter), general relativistic (we include GR consistently both in the stellar structure and in the neutrino transport), spherically symmetric (the stellar structure is determined by integrating the Tolman–Oppenheimer–Volkoff (TOV) equations), and flux limited (we use the diffusion approximation and apply a flux limiter to preserve causality in the optically thin regions near the border). Since we want to focus on how the EOS affects the evolution and the gravitational wave emission, we do not include convection in our simulations (see e.g.[10] for a PNS simulation including convection with the mixing length theory) nor accretion [9,11–13], which are both present in this phase. The spacetime metric is

$$ds^2 = -e^{2\phi}dt^2 + e^{2\lambda}dr^2 + r^2 d\Omega, \tag{34}$$

where ϕ and λ are metric functions that depend on the radius r, t is the time for an observer at infinity, and $d\Omega$ is the element of solid angle.

The stellar structure, at each time step, is given by the TOV equations,

$$\frac{dr}{da} = \frac{1}{4\pi r^2 n_B e^{\lambda}}, \tag{35}$$

$$\frac{dm}{da} = \frac{\epsilon}{n_B e^{\lambda}}, \tag{36}$$

$$\frac{d\phi}{da} = \frac{e^{\lambda}}{4\pi r^4 n_B}(m + 4\pi r^3 P), \tag{37}$$

$$\frac{dP}{da} = -(\epsilon + P)\frac{e^{\lambda}}{4\pi r^4 n_B}(m + 4\pi r^3 P), \tag{38}$$

where r is the radius, m is the gravitational mass at radius r, a is the enclosed baryon number at radius r, ϵ is the total energy density (matter *plus* neutrino energy density), and the metric function λ is given by

$$e^{-\lambda} = \sqrt{1 - \frac{2m}{r}}. \tag{39}$$

The neutrino diffusion equations are [3,34]

$$F_\nu = -\frac{e^{-\lambda}e^{-\phi}T^2}{6\pi\hbar^3}\left(D_3\frac{\partial(Te^{\phi})}{\partial r} + (Te^{\phi})D_2\frac{\partial\eta}{\partial r}\right), \tag{40}$$

$$H_\nu = -\frac{e^{-\lambda}e^{-\phi}T^3}{6\pi\hbar^3}\left(D_4\frac{\partial(Te^{\phi})}{\partial r} + (Te^{\phi})D_3\frac{\partial\eta}{\partial r}\right), \tag{41}$$

$$\frac{\partial Y_L}{\partial t} + \frac{\partial(e^{\phi}4\pi r^2 F_\nu)}{\partial a} = 0, \tag{42}$$

$$T\frac{\partial s}{\partial t} + \mu_{\nu_e}\frac{\partial Y_L}{\partial t} + e^{-\phi}\frac{(e^{2\phi}4\pi r^2 H_\nu)}{\partial a} = 0, \tag{43}$$

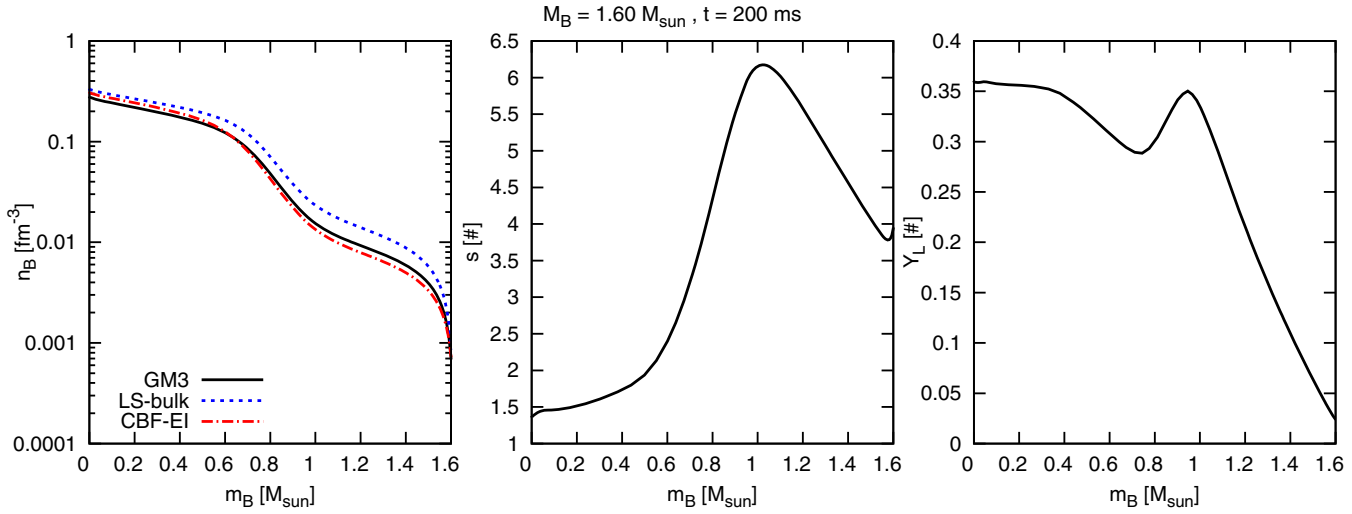

FIG. 5. The initial profiles (at $t = 200$ ms) of the baryon density (left), entropy per baryon (center), and lepton fraction (right) are plotted versus the enclosed baryonic mass for a $M_{\rm B} = 1.60\ M_\odot$ star. The *initial* entropy per baryon and lepton fraction profiles are the same for the three EOSs adopted, whereas the baryon density depends on the EOS (colors and line styles are as in Fig. 2).

where F_ν and H_ν are the neutrino number and energy[3] fluxes, respectively, $\eta = \mu_{\nu_e}/T$ is the electron neutrino degeneracy, and the diffusion coefficients D_2, D_3, and D_4 are given by Eqs. (17), (18), and (19). $Y_L \equiv Y_e + Y_\nu = Y_{e^-} + Y_{\nu_e} - Y_{e^+} - Y_{\bar{\nu}_e}$ is the *total* electron lepton fraction.

Previous PNS studies have found that the beta equilibrium does occur almost everywhere in the star during the evolution [1,3]. Therefore, to additionally simplify the equations, we enforce beta equilibrium [Eq. (14), as in [2]]. We have checked *a posteriori* that beta equilibrium is respected almost everywhere in the star during the evolution, apart for a thin region near the stellar surface at early times (see Appendix B 2).

B. Numerical implementation

In a PNS in beta equilibrium, all thermodynamical quantities can be uniquely determined in terms of three independent variables. A natural choice, looking at the evolution and structure equations, is to use as independent variables the pressure P, the entropy per baryon s, and the lepton fraction Y_L (see Sec. II).

We started the simulation assuming entropy and lepton fraction initial profiles similar to those of Pons *et al.* [3] (see Fig. 5), that is, the profiles obtained in Wilson and Mayle [35] at the end of their core-collapse simulation (200 ms after core bounce). The entropy and lepton fraction content of the PNS depend on the stellar mass. To qualitatively reproduce this behavior, we have rescaled the entropy and lepton fraction profiles with the stellar baryon mass $M_{\rm B}$,

$$s(a, t = 200\ \text{ms}) = \frac{M_{\rm B}}{M'_{\rm B}} s'(a', t = 200\ \text{ms}), \quad (46)$$

$$Y_L(a, t = 200\ \text{ms}) = \frac{M_{\rm B}}{M'_{\rm B}} Y'_L(a', t = 200\ \text{ms}), \quad (47)$$

$$a = \frac{M_{\rm B}}{M'_{\rm B}} a', \quad (48)$$

where the prime refers to the reference profiles of Wilson and Mayle [35]. Using these initial entropy and lepton fraction profiles at 200 ms, we have first determined the initial structure of the star solving the TOV Eqs. (35)–(38) by numerical relaxation ([36], Sec. 17.3). We have then evolved the star solving separately the structure and diffusion equations in a series of iterative predictor-corrector steps, as in [3]. To prevent superluminar fluxes, the neutrino number and energy fluxes [Eqs. (40) and (41)] have been numerically limited using the flux limiter of Levermore and Pomraning [37], which is relevant near the stellar surface, where the matter is optically thin to neutrinos and the diffusion approximation breaks down.

We discuss the numerical convergence of our code in Appendix B 1. More details on the code are reported in [38].

C. Results

We now discuss how the PNS evolution depends on the EOS adopted and the total stellar baryon mass. In Fig. 6 we

[3]Eq. (43) is derived from the sum of the transport equations for the neutrino and matter energy,

$$\frac{\partial e_\nu}{\partial t} - \frac{P_\nu}{n_{\rm B}}\frac{\partial n_{\rm B}}{\partial t} + e^{-\phi}\frac{(e^{2\phi} 4\pi r^2 H_\nu)}{\partial a} = +e^{\phi}\frac{S_E}{n_{\rm B}}, \quad (44)$$

$$\frac{\partial e_{\rm matter}}{\partial t} - \frac{P_{\rm matter}}{n_{\rm B}}\frac{\partial n_{\rm B}}{\partial t} = -e^{\phi}\frac{S_E}{n_{\rm B}}, \quad (45)$$

where S_E is the energy and momentum integrated source term for the energy [3].

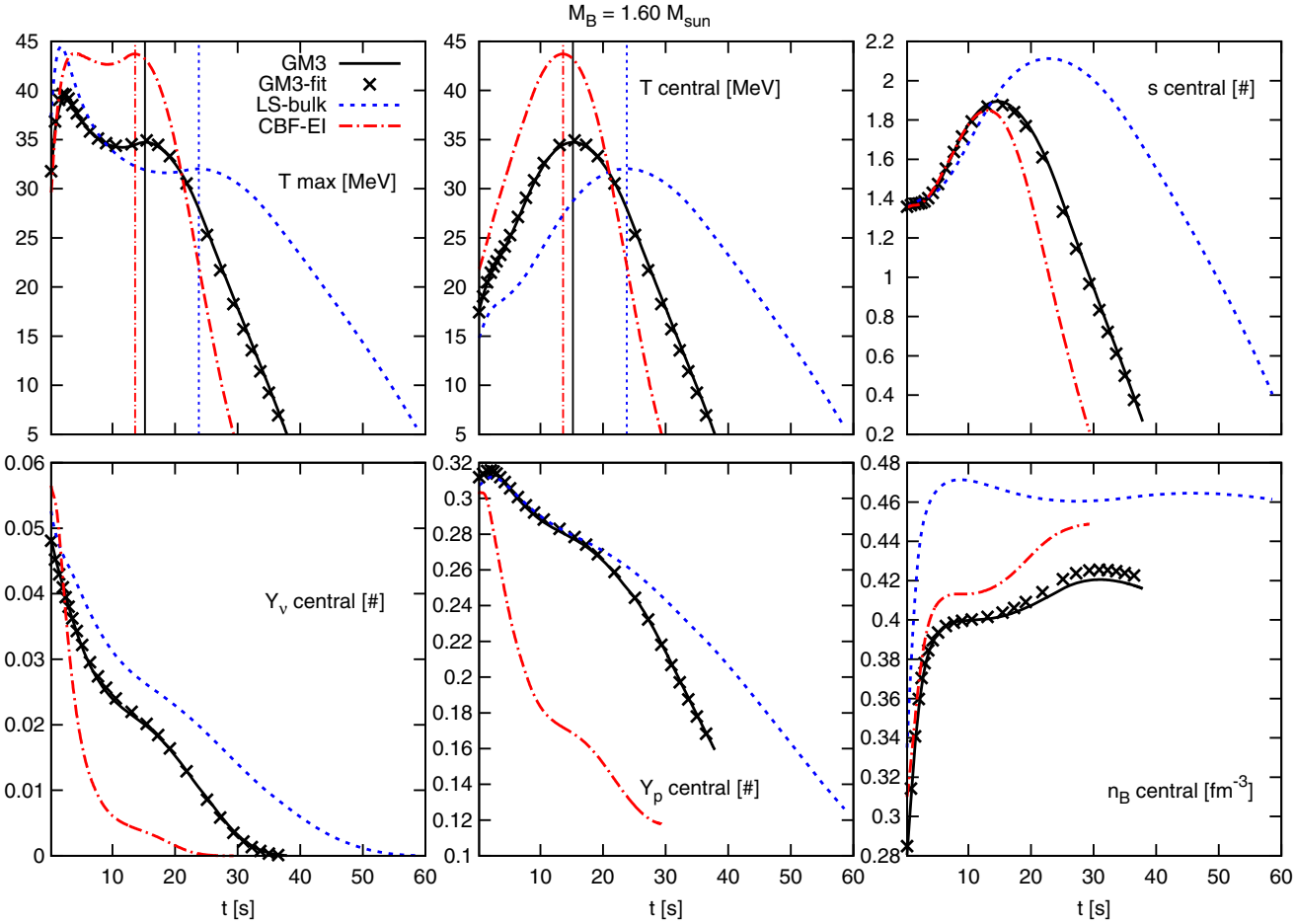

FIG. 6. Time dependence of the maximum and central temperature (left and central upper plots), central entropy per baryon (right upper plot), neutrino and proton fraction (left and central lower plots) and central baryon density (right lower plot), for a star with total baryon mass $M_B = 1.60\ M_\odot$ evolved using the three EOSs. Colors and line styles are as in Fig. 2. The three vertical lines in the temperature plots mark the end of the Joule-heating phase (see text).

show the evolution of the central and maximum temperature, central entropy per baryon, central neutrino and proton fraction, and central baryon density for the three nucleonic EOSs considered in this paper and for the total baryon mass $M_B = 1.60\ M_\odot$. It is apparent that the evolution with the GM3-fit EOS reproduces that with the GM3 EOS. Therefore, in the rest of this paper we do not distinguish between the GM3-fit and GM3 EOS. In Table I we summarize the time scales of the evolutionary phases and the maximum central temperature for the three EOSs and for three stellar baryon masses $M_B = (1.25, 1.40, 1.60)\ M_\odot$. In Fig. 7 we plot the time dependency of the total neutrino luminosity, gravitational mass, and stellar radius of a PNS evolved using the three EOSs discussed in this paper and with the stellar baryon masses $M_B = (1.25, 1.40, 1.60)\ M_\odot$.

The qualitative behavior of the stellar evolution is the same for the three EOSs and the three stellar masses, even though the time scales and the thermodynamical profiles are quantitatively different (Fig. 6 and Table I). At the beginning of the evolution, which is 200 ms from core bounce, the PNS has a (relatively) low entropy core and a high entropy envelope (see Fig. 5). The neutrino chemical potential initially is very high in the center of the star; the process of neutrino diffusion transfers this degeneracy energy from neutrinos to the matter and this causes the heating of the PNS core. Moreover, on time scales of about 10 s, the star contracts from about 30 km to its final radius of about 12–13 km. The region which is affected the most from this contraction is the envelope, whose temperature significantly increases. At the same time, the steep negative neutrino chemical potential gradient in the envelope causes a deleptonization of the envelope. The neutrinos leave the star, bringing with them energy. The joint effect of the envelope heating caused by contraction and the cooling caused by neutrino emission is apparent in the behavior of the maximum stellar temperature: before the central temperature, T_c, reaches its maximum, the maximum temperature reached in the interior of the star, $T_{\max}$, increases, reaches a maximum value, and then decreases (Fig. 6). The initial phase, during which the central temperature

TABLE I. Significant quantities describing the PNS evolution for the three EOSs described in this paper and for three stellar baryon masses. The first column contains the name of the EOS, the second column contains the stellar baryon mass, the third and fourth columns contain the maximum central temperature and the corresponding time (the latter approximately corresponds to the end of the Joule-heating phase), respectively, the fifth column contains the time at which the central neutrino fraction becomes equal to $Y_\nu = 0.005$ (this is an indication on the duration of the deleptonization phase), and the sixth column contains the time at which our simulation ends (namely, when the central temperature becomes equal to $T = 5$ MeV). All simulations start at $t_{\rm start} = 0.2$ s.

EOS	$M_{\rm B}$ $[M_\odot]$	$T_{\rm max}$ [MeV]	$t_{\rm Jh}$ [s]	$t_{\rm del}$ [s]	$t_{\rm end}$ [s]
GM3	1.25	24.6	9.0	13.1	20.8
GM3	1.40	28.7	11.2	18.6	27.1
GM3	1.60	34.9	15.2	27.9	37.7
LS-bulk	1.25	23.6	13.5	17.5	30.6
LS-bulk	1.40	26.6	17.6	26.3	41.0
LS-bulk	1.60	32.1	23.8	41.4	59.2
CBF-EI	1.25	32.3	7.31	3.46	17.0
CBF-EI	1.40	37.0	9.55	5.65	21.6
CBF-EI	1.60	43.7	13.6	11.7	29.4

increases, lasts for several seconds and has been referred to as *Joule heating* phase in previous works [1,2]. We may place the end of this phase approximately at the time T_c reaches its maximum (vertical dotted lines in Fig. 6); at that time the central temperature is also the maximum stellar temperature (see Fig. 6).

After the Joule heating phase, there is a general cooling of the star as the deleptonization proceeds. In [1,2] it was found that the end of the Joule heating phase coincides with the end of deleptonization, whereas in [3], with the GM3 EOS and a more refined treatment of neutrino opacities, it was found that the deleptonization is longer than the Joule-heating phase. We agree with this last result for the stars with the GM3 and LS-bulk EOSs, whereas in the case of the CBF-EI EOS we find that most of neutrinos have been radiated away by the end of the Joule-heating phase (Fig. 6 and Table I).

Our results for the $M_{\rm B} = 1.60\ M_\odot$ PNS with the GM3 EOS are in qualitative agreement with those of [3]. In particular, the duration of the Joule-heating phase is in good agreement (cf. Fig. 6 of this paper with Fig. 17 in [3]); however we find lower stellar temperatures and a shorter cooling phase.

We think that the quantitative differences[4] between our results and those of [3] are due to differences in the initial profiles and in the details of the treatment of the diffusion processes.

For each EOS, the evolutionary time scales are smaller for stars with smaller baryonic mass, see Table I. This is due to the way we have rescaled the initial entropy per baryon and lepton fraction profiles with M_B, but also to the fact that a lower stellar mass corresponds to lower baryonic densities and then to longer neutrino mean-free paths. We also notice that a lower stellar mass corresponds to lower temperatures. This again depends on the initial entropy profiles and on the different densities present in the star, see Fig. 3: at a given entropy per baryon and lepton (or neutrino) fraction, lower densities (i.e., lower masses) correspond to lower temperatures. To simulate a fully consistent PNS evolution, one should use initial profiles generated by core-collapse simulations of stars with the same baryonic mass (see [3] for a study on how the initial conditions affect the PNS evolution).

Figure 3 shows that, at fixed entropy, CBF-EI EOS is hotter than the GM3 EOS, which is hotter than the LS-bulk EOS (see discussion in Sec. II D). Since, for a given stellar mass, the initial entropy profiles are the same for the three EOSs, then the CBF-EI star reaches temperatures higher than the GM3 stars, which in turn reaches temperatures higher than the LS-bulk star, see Fig. 6 and Table I.

The fact that the LS-bulk evolution is slower than the GM3 one, which in turn is slower than that of the CBF-EI EOS, may well be explained by the fact that in the many-body CBF-EI EOS nuclear correlations are stronger than in the mean-field GM3 EOS, in which in turn are stronger than in the LS-bulk EOS (where the baryon masses are equal to the bare ones). A smaller neutrino cross section is a consequence of a greater baryon correlation (Sec. III D). This effect is relevant even at the mean-field level, where one adopts the description of the baryon spectra in terms of effective masses and single-particle potentials to obtain the diffusion coefficients. For example, the fact that the proton effective mass is significantly smaller than the neutron one in the CBF-EI framework is a consequence of the tensor correlations which are stronger in the n-p channel than in the n-n or p-p channels.

To check this interpretation, that is, that the different time scales are mainly due to the details of the microphysics (i.e., the baryon spectra and hence the neutrino mean-free paths and diffusion coefficients), we have run a simulation of a $M_{\rm B} = 1.60\ M_\odot$ PNS with the LS-bulk and CBF-EI EOSs, *but* with the diffusion coefficients of the GM3 EOS. As expected, we find out that the LS-bulk time scale is reduced with respect to that of a self-consistent simulation (i.e., using the LS-bulk diffusion coefficients), and the CBF-EI time scale is increased with respect to that of a self-consistent simulation. Of course, the time scales and the evolutionary profiles found in this nonconsistent manner are not equal to those corresponding to the GM3 EOS, the differences due to the details of the EOSs. Both the EOS

[4]The differences amount to about 10% in the value of the central temperature maximum and of the deleptonization time, and in less than 2% for the time of the end of Joule-heating phase, compare Table I and Fig. 17 of [3].

and the neutrino mean-free paths influence the PNS evolution; in fact, each EOS has a different thermal content and neutrino degeneracy, and different thermodynamical derivatives that determine how the stellar profiles change while energy and leptons diffuse through the star.

D. Neutrino luminosity

In 1987 a supernova (SN1987a) has been observed in the Large Magellanic Cloud [39]. Together with the electromagnetic signal, 19 neutrinos were detected by the Cherenkov detectors Kamiokande II [4] and IMB [5]. These neutrinos have been observed on a time scale of ten seconds, and are therefore thought to have been emitted during the PNS phase. However, they were too few to accurately constrain the emitted neutrino spectrum and its time dependence (see e.g. [40]) and to give unambiguous answers about the proto-neutron star physics [2,3,9,40]. Today, with the current detectors, a SN event such that of 1987 would generate $\sim 10^4$ neutrino detections [41], which would provide valuable information on the physical processes dominating the PNS evolution. It is therefore fundamental to determine how the underlying EOS modifies the PNS neutrino signal.

Our code has some limitations in reconstructing the emitted spectrum; besides the spherical symmetry it assumes: (i) beta equilibrium, (ii) a Fermi distribution for all neutrino species, and (iii) a vanishing chemical potential for the muon and tauon neutrinos everywhere in the star. Assumptions (i) and (ii) are reasonable in the interior of the star, and lose accuracy near the stellar border, where the diffusion approximation breaks down and in practice the fluxes are always flux limited. To obtain a precise description of the neutrino emitted spectrum, one has to employ multiflavor multigroup evolutionary codes (see e.g. [14]), that possibly also account for neutrino leakage near the stellar border. This is outside the aims of our work; however our approximations are reasonable as far as one is interested in total quantities, in particular the total neutrino luminosity L_ν (Fig. 7), which is equal to minus the gravitational mass variation rate,

$$L_\nu = \mathrm{e}^{2\phi(R)} 4\pi R^2 H_\nu(R) = -\frac{\mathrm{d}M}{\mathrm{d}t}, \tag{49}$$

where $H_\nu(R)$ is the neutrino energy luminosity at the stellar border.

We determine the formula to estimate the signal in terrestrial detectors following [9] and applying a slight modification introduced by [3], and we specify our results for the Super-Kamiokande III detector [41,42]. The main reaction that occurs in a water detector like Super-Kamiokande is the electron antineutrino absorption on protons, $\bar{\nu}_e + p \to n + e^+$ [Eq. (1) of [41]]. The number flux of antineutrinos arriving at the detector is given by

$$\frac{\mathrm{d}\mathcal{N}}{\mathrm{d}t} = \frac{\tilde{\sigma}_0 \tilde{n}_p \mathcal{M}}{4\pi D^2} \mathrm{e}^{\phi_\nu} T_\nu L_{\bar{\nu}_e} \frac{G_W(\mathrm{e}^{\phi_\nu} T_\nu, E_{\mathrm{th}})}{7\pi^4/120}, \tag{50}$$

$$G_W = \int_{E_{\mathrm{th}}/T}^{\infty} \frac{x^2 (x - \frac{\Delta}{T}) \sqrt{(x - \frac{\Delta}{T})^2 - (\frac{m_e}{T})^2}}{1 + \mathrm{e}^x} W(xT)\mathrm{d}x, \tag{51}$$

where $\tilde{n}_p \simeq 6.7 \times 10^{31}$ kton^{-1} is the number of free protons (i.e., hydrogen atoms) per *unit water mass* of the detector, $\tilde{\sigma}_0 = 0.941 \times 10^{-43}$ cm^2 MeV^{-2}, $\mathcal{M}$ is the water mass of the detector, D is the SN distance from the detector, G_W is a modified and truncated Fermi integral, E_{th} is the incoming neutrino energy threshold (to cut off the low-energy neutrino background that is a noise for high-energy SN and PNS neutrinos, [41]), Δ_m is the neutron-proton mass difference, m_e is the electron mass, and $W(E)$ is the efficiency of the detector at incoming neutrino energy $E \equiv xT$. e^{ϕ_ν}, T_ν, and $\mu_{\bar{\nu}_e}$ are the redshift, temperature, and antineutrino chemical potential at the neutrinosphere, which is the sphere inside the PNS at whose radius R_ν neutrinos decouple from matter (therefore, $\mathrm{e}^{\phi_\nu} T_\nu$ and $\mathrm{e}^{\phi_\nu} \mu_{\bar{\nu}_e}$ are the temperature and the chemical potential at the neutrinosphere, seen by an observer at infinity).

We take Super-Kamiokande III as reference detector, and therefore $\mathcal{M} \simeq 22.5$ ktons [41], $E_{\mathrm{th}} = 7.5$ MeV, and W is reported in Fig. 3 of [42] and is one for $E > E_{\mathrm{th}}$. We consider a galactic PNS, $D = 10$ kpc, and assume that the neutrinosphere is at the radius at which the (total, of all flavors) neutrino energy flux becomes one third of the (total, of all flavors) neutrino energy density, $H_\nu/\epsilon_\nu = 1/3$. Finally, we take the electron antineutrino energy to be one sixth of the total, $L_{\bar{\nu}_e} = L_\nu/6$, since (i) at the neutrinosphere all neutrino type chemical potentials are very small and (ii) we do not account for neutrino oscillations (which would enhance the flux by about 10% [41]).

The neutrino signal rate and total signal for the three EOSs are shown in Fig. 8. Since the binding energies of the cold neutron star of the three EOSs we consider are very similar (see Fig. 7), the total energies emitted by neutrinos during the PNS evolution are very similar too. On the other hand, the rate of antineutrino emission and the temperature at the neutrinosphere varies according to the underlying EOS. Therefore, there is an EOS signature on the cumulative antineutrino detection. The signal of the CBF-EI PNS is noticeably larger than the other EOSs, even though its gravitational binding energy at the end of the evolution is between those of the LS-bulk and GM3 EOSs (Fig. 7). This is due to the fact that the higher temperatures of the CBF-EI EOS cause a smoother antineutrino distribution function at the neutrinosphere, and hence more antineutrinos have an energy greater than the threshold E_{th} at the detector.

The different evolutionary time scales for the three EOSs and stellar masses correspond to different signal time scales, which may easily be inferred from the antineutrino detection rate. The antineutrino detection rates for the three

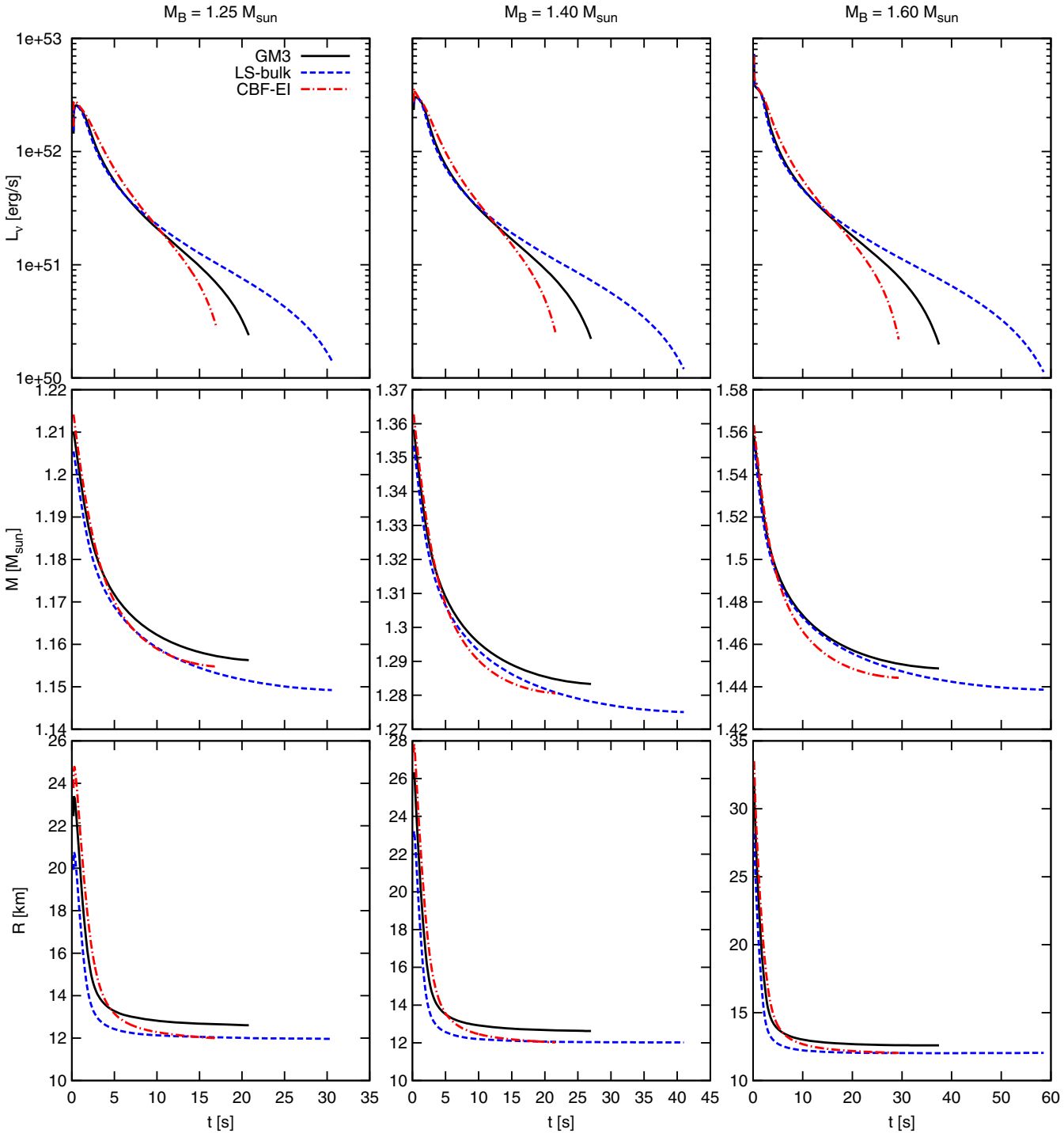

FIG. 7. Time dependence of the total neutrino luminosity (upper panels), gravitational mass (middle panels), and stellar radius (lower panels) of a PNS evolved with the three EOSs considered in this paper and the baryon stellar masses $M_B = (1.25, 1.40, 1.60)\ M_\odot$. The black solid lines correspond to the GM3 EOS determined through the fit and the procedure described in Sec. II C, the blue dashed lines to the LS-bulk EOS, and the dot-dashed red lines to the CBF-EI EOS. The gravitational masses at the end of the simulations are: for $M_B = 1.25\,M_\odot$, $M_{GM3} = 1.1554\,M_\odot$, $M_{LS-bulk} = 1.1492\,M_\odot$, $M_{CBF-EI} = 1.1548\,M_\odot$; for $M_B = 1.40\ M_\odot$, $M_{GM3} = 1.2824\ M_\odot$, $M_{LS-bulk} = 1.2750\ M_\odot$, $M_{CBF-EI} = 1.2806\ M_\odot$; and for $M_B = 1.60\ M_\odot$, $M_{GM3} = 1.4478\ M_\odot$, $M_{LS-bulk} = 1.4386\ M_\odot$, $M_{CBF-EI} = 1.4442\ M_\odot$.

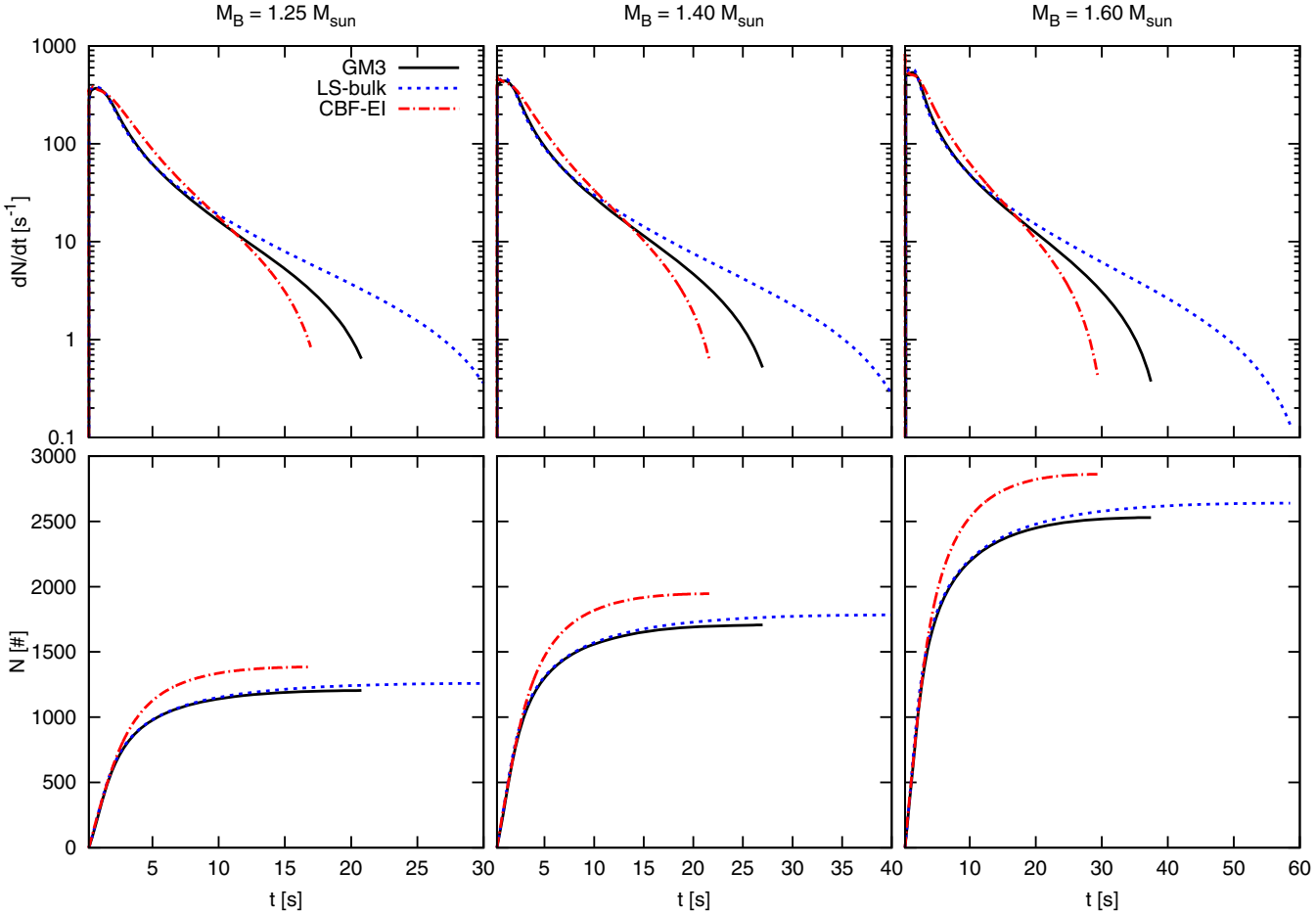

FIG. 8. Signal in the Super-Kamiokande III Cherenkov detector, for the three EOSs considered in this paper. In the top panels, electron antineutrino detection rate; in the bottom panels, electron antineutrino cumulative detection. In the left plots, we consider a star with $M_{\rm B} = 1.25\ M_\odot$, in the central plots $M_{\rm B} = 1.40\ M_\odot$, and in the right plots $M_{\rm B} = 1.60\ M_\odot$. Colors and line styles are as in Fig. 7.

EOSs and the three stellar masses are qualitatively very similar. During the first ten seconds the LS-bulk and GM3 stars have very similar detection rates; at later times, the detection rates become different, because the LS-bulk star has a longer evolution than the GM3 star. The CBF-EI star, instead, has the peculiarity of maintaining a higher antineutrino emission rate during the Joule-heating phase (approximately, during the first ten seconds), which is due to the faster deleptonization that we have already discussed in Sec. IV C and to higher temperatures.

V. GRAVITATIONAL WAVES FROM QUASINORMAL MODES

A supernova explosion is a highly energetic event and the PNS which is formed as a remnant is expected to oscillate wildly. The relativistic theory of stellar perturbations [43,44] predicts the existence of stellar oscillation modes, the so-called quasinormal modes (QNMs), through which the star loses energy emitting gravitational waves (GWs). To find the frequencies of these modes, in the case of a spherical, nonrotating star, Einstein's equations are perturbed about the background (34), and the perturbed functions are expanded in spherical harmonics and Fourier transformed. Thus, the spacetime metric describing the perturbed spacetime can be written as[5]

$$\begin{aligned} {\rm d}s^2 = &-{\rm e}^{2\phi}(1 + r^l H_0 Y_{lm} {\rm e}^{\imath\omega t + \imath m\varphi}){\rm d}t^2 \\ &- 2\imath\omega r^{l+1} H_1 Y_{lm} {\rm e}^{\imath\omega t + \imath m\varphi} {\rm d}t{\rm d}r \\ &+ {\rm e}^{2\lambda}(1 - r^l H_0 Y_{lm} {\rm e}^{\imath\omega t + \imath m\varphi}){\rm d}r^2 \\ &+ r^2(1 - r^l K Y_{lm} {\rm e}^{\imath\omega t + \imath m\varphi}){\rm d}\Omega, \end{aligned} \tag{52}$$

where $Y_{lm}(\vartheta, \varphi)$ are the scalar spherical harmonics and $H_0(r,\omega)$, $H_1(r,\omega)$, $K(r,\omega)$ describe the polar metric perturbations. A fluid element in a point x^μ is displaced by the perturbation in the new position $x'^\mu = x^\mu + \xi^\mu$, where the displacement vector ξ^μ can be written as

$$\xi^t = 0, \tag{53}$$

[5]We use the gauge adopted in [43].

$$\xi^r = r^{l-1}\mathrm{e}^{-\lambda}W(r,\omega)Y_{lm}(\theta,\varphi)\mathrm{e}^{\imath\omega t+\imath m\varphi}, \tag{54}$$

$$\xi^\theta = -r^{l-2}V(r,\omega)\partial_\theta Y_{lm}(\theta,\varphi)\mathrm{e}^{\imath\omega t+\imath m\varphi}, \tag{55}$$

$$\xi^\varphi = -\frac{r^{l-2}V(r,\omega)}{\sin^2\theta}\partial_\varphi Y_{lm}(\theta,\varphi)\mathrm{e}^{\imath\omega t+\imath m\varphi}. \tag{56}$$

The perturbations of the energy density and pressure of the fluid composing the star are expanded in the same way. Due to the decomposition in spherical harmonics and to the Fourier expansion, the linearized Einstein + hydro equations do separate, and are reduced to a set of coupled, linear ordinary differential equations for the radial part of the perturbed fluid and of the metric functions.

A QNM is defined as a solution of the perturbed equations which is regular at the center, continuous at the stellar surface, and which behaves as a purely outgoing wave at radial infinity. The set of discrete values of the complex frequency $\omega = 2\pi\nu + \imath/\tau$ for which these conditions are satisfied are the QNM eigenfrequencies: the real part is the pulsation frequency ν, the imaginary part is the inverse of the damping time τ.

The QNMs are classified according to the nature of the restoring force which prevails in bringing back the perturbed fluid element to the equilibrium position. For the p_n-modes, or "pressure modes," ($n = 1, 2, \ldots$) the main restoring force is due to pressure; for the g_n-modes ($n = 1, 2, \ldots$), or "gravity modes," the main restoring force is buoyancy. The order n of the mode corresponds to the number of nodes of the radial eigenfunction of the displacement vector. The f-mode, i.e., the fundamental mode of the star, describes the global pulsation motion of the fluid, and has no radial nodes. In a cold neutron star, typical values for the QNM frequencies and damping times are $\nu_f \simeq 1.5$–2.5 kHz, $\tau_f \simeq 0.1$ s, $\nu_{p_1} \simeq 5$–10 kHz, and $\tau_{p_1} = 1$–10 s. The g-modes are due to the presence of thermal and/or composition gradients; in absence of composition gradients, all g-modes of a cold neutron star degenerate to zero frequency. Conversely, they are present in a PNS [15,17], as we shall show below.

To determine the quasinormal mode frequencies at a given time t of the stellar evolution, we have first evolved the PNS, finding the profiles of the pressure $P(r,t)$, the energy density $\epsilon(r,t)$, the baryon number density $n_{\mathrm{B}}(r,t)$, and the sound speed, $c_s(r,t)$, for the three EOSs and the different values of the baryonic mass we consider in this paper. Then we have determined the "effective barotropic EOS" by inverting the pressure-radius profile, thus finding $r = r(P,t)$ and then $\epsilon^{\mathrm{eff}}(P;t) = \epsilon(r(P,t),t)$ and $c_s^{\mathrm{eff}}(P;t) = c_s(r(P,t),t)$. Using these expressions, we have solved the equations of stellar perturbations (we used the formulation of [45]), to find the frequencies and damping times of the first p- and g-modes and of the fundamental mode.

A. Results of the numerical evolution

We have evolved three stellar models with baryon masses (1.25, 1.40, and 1.60 $M_\odot$) and the EOSs LS-bulk, CBF-EI and GM3, which was used in [15]. For this EOS, the QNM frequencies we compute for the 1.60 $M_\odot$ star agree with those of "model A" of [15] within a few percent. We think that the small differences between our results and those of [15] are due to differences in the initial profiles and in the details of the treatment of the diffusion processes. The numerical values of the f-, g_1- and p_1-QNM frequencies and damping times are tabulated in Appendix C.

In Fig. 9 we show, as an example, how the QNM frequencies and damping times change during the first five seconds of the PNS life. The plots are given for the three EOSs we consider, and for a star with baryonic mass $M_{\mathrm{B}} = 1.40\ M_\odot$ as an example.

In the upper panel we show the frequency of the g_1- and of the f-modes, in the middle panel the frequency of the mode p_1, and in the lower panel the damping time of the three modes. From the upper panel of Fig. 9 we see that during the first second, ν_{g_1} approaches ν_f, but they never cross. At later times, ν_{g_1} increases, reaches a maximum and then decreases, whereas ν_f does the opposite: it reaches a minimum slightly before ν_{g_1} reaches its maximum, and then increases toward the asymptotic value of the corresponding cold neutron star. This behavior is a general feature of the three EOS; however, the minimum (maximum) of ν_f (ν_{g_1}) occurs at different times for different EOSs. In addition frequencies belonging to different EOSs differ, at each time, as much as ∼100–200 Hz. ν_{p_1} also has a minimum (which was not found in [15]), at earlier times with respect to ν_f and ν_{g_1}.

It may be noted that our results are qualitatively different from those of [17,18], where the QNMs show a monotonic increase of the f- and p-modes, and a monotonic decrease of the g-mode. We think that this is due to the fact that a consistent evolution of the PNS is crucial to describe the behavior of the QNMs.

The time dependence of the QNM frequencies described above would produce differences in the gravitational waveforms emitted by the PNS which, if detected, would provide valuable information on the underlying EOS. The waveform emitted by a star oscillating in a QNM with frequency ν and damping time τ can be written as $h(t) = h_0\mathrm{e}^{-(t-t_0)/\tau}\sin[2\pi\nu(t-t_0)]$, where h_0 is the initial amplitude and t_0 some initial time. Since the mode energy is proportional to the square of the wave function, $E_{\mathrm{QNM}} \propto \mathrm{e}^{-2(t-t_0)/\tau}$, and the gravitational wave (GW) luminosity is $L_{\mathrm{GW}} = -\dot{E}_{\mathrm{QNM}} \simeq \frac{2E_{\mathrm{QNM}}}{\tau}$. Therefore, QNMs with smaller damping times are more effective in extracting energy from the PNS in the form of GWs. In a cold star $\tau_f < \tau_p$, and this means that the energy will be radiated mainly at the frequency of the fundamental mode. However, during the first second of the PNS life the

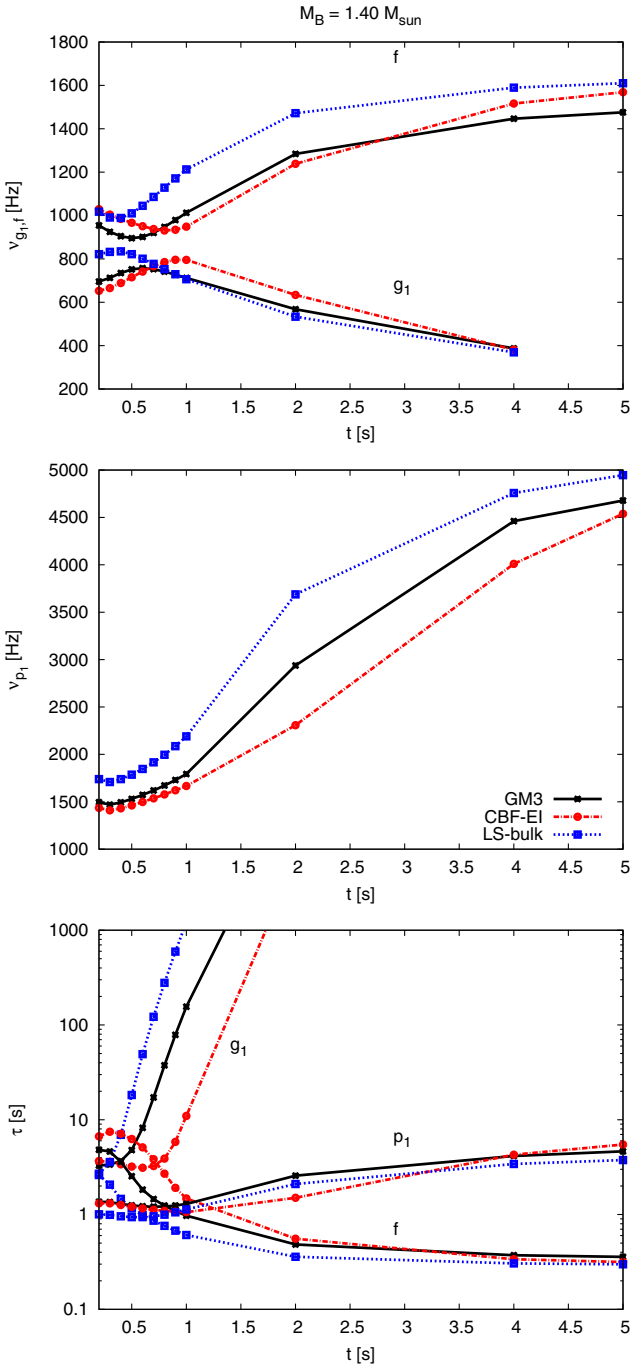

FIG. 9. Time dependence of the PNS quasinormal mode frequencies and damping times for the three EOSs and for $M_B = 1.40\ M_\odot$.

situation is quite different; the lower panel of Fig. 9 shows that the p_1-mode has a damping time $\tau_{p_1} \simeq 1$ s, *smaller* than that of the f- and of the g_1-modes, and it can be *more effective* in radiating energy than the fundamental and the first g-mode. After the first second, the fundamental mode becomes the more efficient GW emitter.

It should be stressed that the mechanical energy of a newly born PNS is dissipated in gravitational waves only in part. GWs compete with other dissipative mechanisms associated to neutrino diffusion; therefore, gravitational waves will be emitted by a PNS only if τ_{GW} is smaller than the dissipation time scales typical of neutrino diffusion. These have been estimated to be of the order of $\tau_\nu \sim 10$–20 s (see [15] for a discussion on this issue and references therein). From the lower panel of Fig. 9 we see that the damping times of the f- and p_1-modes are always smaller than τ_ν, whereas τ_{g_1} becomes larger than τ_ν after the first few tenths of seconds. Thus, if the PNS has a significant amount of mechanical energy to release, we can reasonably expect that a part of it will be released in gravitational waves.

Recent 3D simulations of the early explosion phase of core-collapse supernovae and of the following accretion phase [46,47] show that other phenomena than stellar oscillations may contribute to gravitational wave emission; for instance, standing accretion shock instability and convection, which are shown to be associated to stochastic oscillations, and to unstable g-modes, different from the stable g-modes considered in this paper. For a review see also [48].

B. A fit of the fundamental and first p-mode periods

In nonrelativistic variable stars (as Chepheids), the ratio of the periods $P_1/P_0 = \nu_f/\nu_{p_1}$ of the first overtone (that corresponds in the language of stellar oscillations in GR to the first p-mode) and of the fundamental mode is a function of the quantity $Q_0 = P_0\sqrt{\bar{\rho}/\rho_\odot}$, where $P_0 = \nu_f^{-1}$ and $\rho_\odot = 2.97 \times 10^{-18}\ M_\odot/\mathrm{km}^3$ is the mean Sun density (see e.g. [49]). We have fitted the ratio $P_1/P_0 \equiv \nu_f/\nu_{p_1}$ with a linear dependence on $Q_0 \propto \sqrt{\bar{\rho}}/\nu_f$, obtaining

$$\frac{P_1}{P_0} = 1.1131(\pm 0.0066) - 1596(\pm 17)\frac{P_0}{1\,\mathrm{s}}\sqrt{\bar{\rho}\frac{10^3\,\mathrm{km}}{1\,M_\odot}}. \quad (57)$$

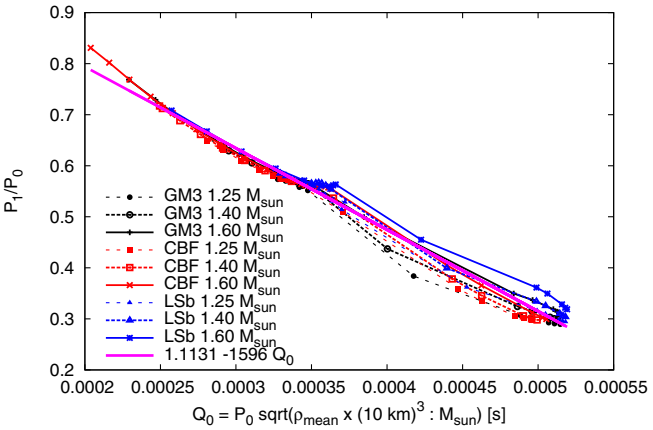

FIG. 10. Ratio between the first p-mode period and the fundamental period as a function of the quantity Q_0, for a PNS in the configurations studied in this paper. The points at the top-left correspond to late evolutionary times, whereas the initial configurations are in the bottom right. See text for details.

The result of the fit is shown in Fig. 10; the corresponding reduced chi square is rather low: $\tilde{\chi} = 3.2 \times 10^{-4}$. This is an indication that, even in PNSs, the ratio P_1/P_0 could be a universal property, independent of the masses and EOSs of the PNS.

VI. CONCLUSIONS

In this paper we have studied the evolution and the gravitational wave emission of a proto-neutron star in the Kelvin-Helmholtz phase, which is the period of the neutron star life subsequent to the supernova explosion, until the star becomes transparent to neutrinos. To perform such a study, we have written a new general relativistic, one-dimensional, energy-averaged, and flux-limited PNS evolutionary code which evolves a general EOS consistently. In particular, we have considered three nucleonic EOSs and three stellar masses, and we have determined the neutrino cross sections self-consistently with the corresponding EOS. The EOSs considered are all nucleonic (without hyperons) and are obtained (i) by the extrapolation from the measured nuclear properties (the LS-bulk EOS [19]), (ii) by the nuclear relativistic mean-field theory (the GM3 EOS [23]), and (iii) by the nuclear nonrelativistic many-body theory (the CBF-EI EOS [20,21]). We have determined the frequencies of the quasinormal oscillation modes for the different EOSs and stellar masses using the general relativistic stellar perturbation theory.

The main improvements with respect to previous works introduced by our study are the following:

(i) We have developed and tested a new fitting formula for the interacting part of the baryon free energy (i.e., neutrons plus protons), which is valid for high density matter, finite temperature, and arbitrary proton fractions. We used this fitting formula to derive the other thermodynamical quantities. This formula is suitable to be used in evolutionary codes.

(ii) We have computed the neutrino cross sections for the many-body theory EOS of [20,21]. They have been computed at the mean-field level [32], that is, the interaction between baryons has been accounted for modifying the baryon energy spectra by means of density-, temperature-, and composition-dependent effective masses and single-particle energies.

(iii) We used these neutrino cross sections to evolve the PNS with the many-body EOS in a consistent way. To our knowledge, this is the first time that a PNS with a many-body EOS has been evolved with consistently determined neutrino opacities. From this evolution, we have determined the stellar quasinormal modes.

Our main results are the following:

(i) The PNS evolution depends on the adopted EOS. In particular, for the many-body EOS CBF-EI the PNS cooling is faster than that with the mean-field EOS GM3, which in turn is faster than that with the extrapolated EOS LS-bulk. In the extrapolated EOS LS-bulk the effective baryon masses have been assumed to be equal to the bare ones, and the result is that this EOS is "less interacting" than the others in the computation of the neutrino cross sections.

(ii) The deleptonization of the PNS with the CBF-EI EOS is almost completed at the end of the Joule-heating phase (similarly to what was found in the first PNS numerical studies by [1,2]), whereas the deleptonization for the GM3 and LS-bulk EOSs proceeds during the cooling phase (as found in [3]). Pons *et al.* [3] explained this difference with the oversimplifications in the treatment of the neutrino opacities in [1,2]. However, we compute the neutrino cross sections for the CBF-EI and the other EOSs with the same procedure of [3]. Therefore, the faster deleptonization is a feature also due to the EOS properties and not only to the treatment of neutrino opacities.

(iii) The total number of electron antineutrinos detected depends on the gravitational binding energy but is not completely determined by it. In particular, the CBF-EI EOS has more antineutrinos detected than the LS-bulk EOS, even though its binding energy is smaller. This is due to the fact that the PNS with CBF-EI EOS has higher temperatures than those with the other EOSs, hence the electron antineutrino distribution function at the neutrinosphere is smoother and more antineutrinos have energies larger than the detector energy threshold. This result remarks the importance of an accurate modeling of the PNS evolution in order to extract information on the PNS physics from the neutrino signal.

(iv) We show that during the first second, the frequencies at which the PNS oscillates emitting gravitational waves have a nonmonotonic behavior. The fundamental mode frequency decreases, reaches a minimum and then increases toward the value corresponding to the cold neutron star which forms at the end of the evolution. The frequency of the first g-mode increases, reaches a maximum and then decreases to the asymptotic zero limit, that of the mode p_1 has a less pronounced minimum at earlier times with respect to the f-mode. We show that this behavior, already noted in [15] for the EOS GM3, is a generic feature when the PNS evolution is consistently described, and that the time scale depends on the EOS. Indeed the time needed to reach the minimum (maximum) for the f- (g_1-)mode can differ by as much as half a second for the EOS we consider.

During the first second, the damping time of all modes is shorter than the neutrino diffusive time scale ($\sim$10 s); therefore gravitational wave emission may be competitive in subtracting energy from the star. This remains true at later times only for the fundamental mode and for the first p-mode.

However, the damping time of the f-mode is much shorter, thus we should expect that after the first few seconds gravitational waves will be emitted mainly at the corresponding frequency.

(v) The QNM frequencies depend not only on the EOS, but also on the stellar baryon mass. In particular, we find that for a lower mass, at the beginning the p_1-mode has higher frequency; for instance, for the 1.25 $M_\odot$ star it approaches 2 kHz.

(vi) We have found a relation between the fundamental and first p-mode frequencies and the mean stellar density [Eq. (57)] which is valid during all PNS phases for the cases considered in this paper. This may be a universal property of PNSs, independent of the mass and the EOS.

This paper may be improved in several directions. About the microphysics, improvements may be done to the neutrino cross section treatment, for example including the effects of collective excitations [50,51] and the weak magnetism correction [52]. Consistently computed neutrino cross sections in the many-body theory for finite temperature and high density matter would be welcome too. About the EOS, it would be interesting to include more physical ingredients, like hyperons and the presence of a crust (alpha particles and a lattice). However, we do not expect dramatic changes for the inclusion of a crust since we have checked that alpha particles do form only near the stellar surface and towards the end of our simulations (Appendix B 3). About the PNS evolution, it would be interesting to abandon the request of beta equilibrium (even though, we have checked that beta equilibrium is almost respected in most of the star, apart for a region near the stellar layer at the beginning of the simulation, see Appendix B 2 and [1,3]) and to allow for the presence of muons and tauons, accounting for the transport of their relative lepton numbers. A major improvement to our work would be the inclusion of accretion [9,11–13] and convection [10], which could have an important effect on the evolution. Finally, we are using as initial configurations the final profile obtained from an old simulation [35], conveniently rescaling it with the total stellar mass. This brings a significant amount of uncertainties; to increase the accuracy of the evolution it would be important to consistently use the final profiles of more modern core-collapse simulations.

ACKNOWLEDGMENTS

This work has been partially supported by "NewCompStar," COST Action MP1304, by the H2020-MSCA-RISE-2015 Grant No. StronGrHEP-690904, by INFN (through grant TEONGRAV), and supported in part by the U.S. Department of Energy, Office of Science, Office of Nuclear Physics, under Contract No. DE-AC02-06CH11357 (A. L.). J. A. P. acknowledges support by the Spanish MINECO Grant No. AYA2015-66899-C2-2-P.

APPENDIX A: FITTING PROCEDURE

The fit has been performed using a set of points on an evenly spaced Cartesian $11 \times 50 \times 12$ grid in $(Y_p; T; n_B)$, from $(0; 1\ \mathrm{MeV}; 0.04\ \mathrm{fm}^{-3})$ to $(0.5; 50\ \mathrm{MeV}; 0.48\ \mathrm{fm}^{-3})$, with steps of $(0.05; 1\ \mathrm{MeV}; 0.04\ \mathrm{fm}^{-3})$. The fit is strictly valid for $n_B \in (0.04; 0.48)\mathrm{fm}^{-3}$ and $T \in (1; 50)$ MeV, but its analytic form is suitable to be used also for $n_B < 0.04\ \mathrm{fm}^{-3}$ and $T < 1$ MeV, see Sec. II B. First, we have fitted *only* the interacting free energy f_B^I, computing the root mean square σ_f. We have done the same for the interacting entropy and pressure, obtaining the root mean squares σ_s and σ_P. Then, we have *simultaneously* fitted the interacting free energy, entropy, and pressure, giving to each fitting point p_i a uniform error $\sigma_{i=\{f;s;P\}}$ that depends on which quantity that point is describing (the free energy, the entropy, or the pressure). The result of the fit of the GM3 and CBF-EI EOS is shown in Table II. We have tried to include in the fit also the second order derivatives, $\partial^2 f_B/\partial T^2$, $\partial^2 f_B/\partial n_B^2$, and $\partial^2 f_B/\partial T \partial n_B$, but the resulting fit did not improve its accuracy.

We have checked that in the range we consider, the fits for the GM3 and the CBF-EI EOSs satisfy the thermodynamic stability conditions [Eqs. (13) and (14) of [24]]

TABLE II. Interacting baryon free energy per baryon fitting parameters, Eqs. (10) and (11). In the first column, we report the fitting coefficient for SNM and PNM, in the second and third columns we report the results of the fit for the GM3 and CBF-EI EOSs, in the fourth and last column, we report the polynomial that is multiplied by that coefficient in the fitting formula. In the last two rows we report the number of points used in the fit and the reduced chi squared. Energies are in MeV and lengths in fm.

Coefficient	GM3	CBF-EI	Polynomial
$a_{1,\mathrm{SNM}}$	−402.401	−284.592	$4Y_p(1-Y_p)n_B$
$a_{2,\mathrm{SNM}}$	1290.54	676.121	$4Y_p(1-Y_p)n_B^2$
$a_{3,\mathrm{SNM}}$	−1540.52	−662.847	$4Y_p(1-Y_p)n_B^3$
$a_{4,\mathrm{SNM}}$	903.8	667.492	$4Y_p(1-Y_p)n_B^4$
$a_{5,\mathrm{SNM}}$	0.0669357	0.112911	$4Y_p(1-Y_p)n_B T^2$
$a_{6,\mathrm{SNM}}$	−0.000680098	−0.00124098	$4Y_p(1-Y_p)n_B T^3$
$a_{7,\mathrm{SNM}}$	−0.0769298	−0.148538	$4Y_p(1-Y_p)n_B^2 T^2$
$a_{8,\mathrm{SNM}}$	0.000915968	0.00192405	$4Y_p(1-Y_p)n_B^2 T^3$
$a_{1,\mathrm{PNM}}$	−274.544	−121.362	$(1-2Y_p)^2 n_B$
$a_{2,\mathrm{PNM}}$	1368.86	101.948	$(1-2Y_p)^2 n_B^2$
$a_{3,\mathrm{PNM}}$	−1609.15	1079.08	$(1-2Y_p)^2 n_B^3$
$a_{4,\mathrm{PNM}}$	916.956	−924.248	$(1-2Y_p)^2 n_B^4$
$a_{5,\mathrm{PNM}}$	0.0464766	0.0579368	$(1-2Y_p)^2 n_B T^2$
$a_{6,\mathrm{PNM}}$	−0.000388966	−0.000495044	$(1-2Y_p)^2 n_B T^3$
$a_{7,\mathrm{PNM}}$	−0.0572916	−0.0729861	$(1-2Y_p)^2 n_B^2 T^2$
$a_{8,\mathrm{PNM}}$	0.00055403	0.000749914	$(1-2Y_p)^2 n_B^2 T^3$
N	19782	18686	
$\tilde{\chi}$	4.18	2.05	

$$\left.\frac{\partial s_{\mathrm{B}}}{\partial T}\right|_{n_{\mathrm{B}}} > 0, \tag{A1}$$

$$\left.\frac{\partial P_{\mathrm{B}}}{\partial n}\right|_{T} > 0. \tag{A2}$$

APPENDIX B: CODE CHECKS

In this Appendix we show the checks of the accuracy of the code, and we justify *a posteriori* the assumption of beta equilibrium and the assumption of a baryon EOS made of an interacting gas with neither alpha particles nor a solid crust. For simplicity, we show the results of a PNS evolved with the CBF-EI EOS and with total baryon mass $M_{\mathrm{B}} = 1.60\ M_{\odot}$; the results for the other EOSs and the other baryon masses are similar.

1. Energy and lepton number conservation

The total energy and other quantum numbers (i.e., the baryon number) are conserved in every physical process. Our code enforces the conservation of the total baryon number $A = M_{\mathrm{B}}/m_n$, but as it evolves, the PNS loses energy and lepton number since neutrinos are allowed to escape from the star. Since the total energy of a star (matter *plus* neutrinos) in spherical symmetry is given by its gravitational mass M, the total energy of the system (stellar energy *plus* energy of the emitted neutrinos) is given by

$$E_{\mathrm{total}} = M(t) + \int_{200\ \mathrm{ms}}^{t} L_{\nu}(t)\mathrm{d}t, \tag{B1}$$

where L_{ν} is defined in Eq. (49). Similarly, for the electron lepton number,

$$N_{\mathrm{total}} = N_L(t) + \int_{200\ \mathrm{ms}}^{t} 4\pi R^2 \mathrm{e}^{\phi(R)} F_{\nu}(R)\mathrm{d}t, \tag{B2}$$

$$N_L = \int_0^A Y_L(a)\mathrm{d}a, \tag{B3}$$

where N_L is the total number of electronic leptons in the star, and F_{ν} is the electron neutrino number flux (we do not account for the other lepton numbers since we do not include muons and tauons in the EOSs and moreover $\mu_{\nu_{\mu}} = \mu_{\nu_{\tau}} = 0$).

Since the conservation of E_{total} and N_{total} has not been enforced, they provide a test for our simulations. From Fig. 11 and from the top plot of Fig. 12, it is clear that they are conserved better than about 0.03% during the evolution.

In Fig. 12 we show, for different *fixed* time steps and for different grid *dimensions*, the total and instantaneous energy conservation from 0.2 to 1 s. The instantaneous energy fractional conservation is defined as

$$\mathrm{i.e.f.c.} = \frac{|\dot{M} + L_{\nu}|}{L_{\nu}}. \tag{B4}$$

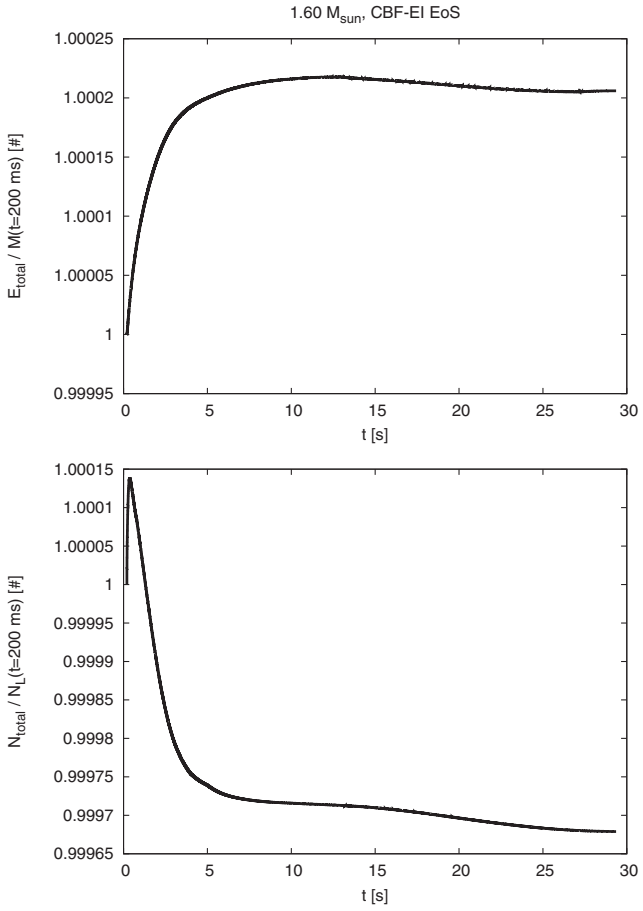

FIG. 11. Total energy E_{total} and total lepton number N_{total} conservation for a PNS with the CBF-EI EOS and 1.60 $M_{\odot}$ baryon mass, normalized with the stellar initial energy and lepton number (our simulations start at 200 ms, see Sec. IV B). The time step is changed during the evolution in such a way that the relative variation in a time step of the profiles of entropy per baryon and lepton fraction is approximately equal to 10^{-4}.

We see that reducing the time step the energy conservation is improved. The instantaneous energy fractional conservation as a function of time shows regular spikes, whose number doubles (triples) if we double (triple) the grid points, and whose magnitude is approximately inversely proportional to the time step. We explain these spikes with the nonlinearity of the transport Eqs. ([36], Sec. 19.1). In fact, the temperature and the neutrino degeneracy appear inside and outside the gradients in the transport equations [Eqs. (40)–(43)]. As a consequence, the power in the Fourier space is accumulated in the shorter wavelengths and is finally released in the longer wavelengths of the solution. This explains why the frequency of the peaks changes with the grid spacing. The spikes of the instantaneous energy conservation have magnitudes which increase when the time step is lowered, since one is dividing over a smaller time step an approximately constant energy jump, $[M(t + \mathrm{d}t) - M(t)]/\mathrm{d}t$. These spikes do not undermine the

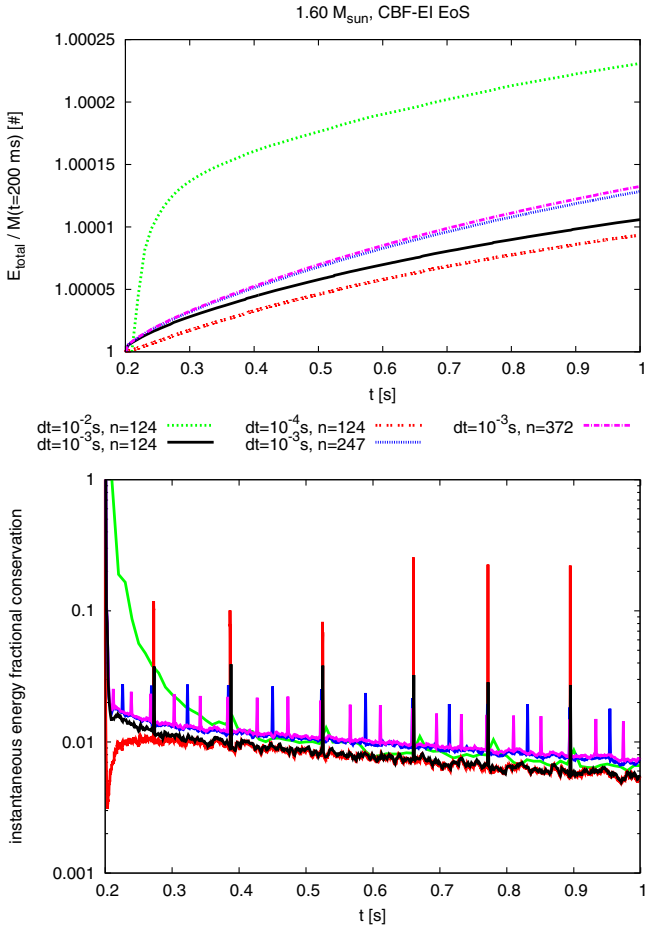

FIG. 12. Total energy $E_{\rm total}$ (normalized with the stellar initial energy) and instantaneous energy fractional conservation for a PNS with the CBF-EI EOS and 1.60 $M_\odot$ baryon mass. The time step `dt` is kept fixed during the evolution and `n` is the number of grid points. The plots begin at 200 ms because this is the initial time of our simulations (see Sec. IV B).

overall conservation of the energy and lepton number and the PNS evolution, see Fig. 11 and upper plot of Fig. 12.

2. Beta equilibrium

Our code (as in [2]) assumes beta equilibrium, Eq. (14). This approximation is valid if the time scale of the beta equilibrium is shorter than the dynamical time scale. We estimate the beta equilibrium time scale using Eqs. (16) and (17a) of [1],

$$t_{\rm beta} = \frac{1}{D_n}, \tag{B5}$$

$$D_n = 1.86\times 10^{-2} Y_p T^5 [S_4(\eta_e) - S_4(\eta_\nu)] \cdot \frac{1-{\rm e}^{-\Delta/T}}{1-{\rm e}^{-\eta_e+\eta_\nu}} \frac{\rm neutrinos}{\rm baryon\cdot s}, \tag{B6}$$

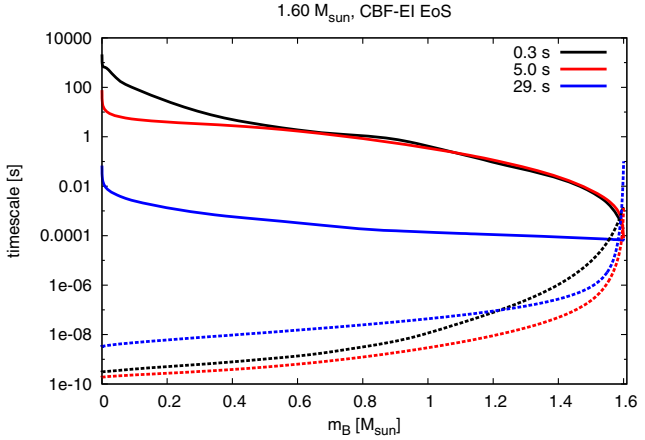

FIG. 13. Dynamical time scale (solid lines) and beta equilibrium time scale (dashed lines) profiles at different times for a PNS with the CBF-EI EOS and 1.60 $M_\odot$ stellar mass.

$$S_4(y) = \frac{y^5}{5} + 2\pi^2\frac{y^3}{3} + 7\pi^4\frac{y}{15}, \tag{B7}$$

where D_n is the net rate of production of electron neutrinos, $\eta = \mu/T$ is the degeneracy parameter, and $\Delta = 0$ in the case of beta equilibrium (we refer the reader to [1] for more details). Since we have assumed beta equilibrium, we put $1-\exp(-\Delta/T) \equiv 1$ to estimate the corresponding time scale. This means that the value of the beta equilibrium time scale is not fully consistent.

Since the PNS structure changes due to how neutrinos transfer energy and lepton number through the stellar layers, we estimate the dynamical time scale with the formula

$$t_{\rm dyn} = R\frac{n_\nu(r)}{F_\nu(r)}, \tag{B8}$$

where $n_\nu(r)$ and $F_\nu(r)$ are the neutrino number density and number flux, respectively (which depend on the radial coordinate r), and R is the stellar radius (notice that F_ν/n_ν has the dimensions of a velocity).

In Fig. 13 we plot the dynamical and beta equilibrium time scales for a PNS with the CBF-EI EOS and $M_{\rm B} = 1.60\ M_\odot$. The beta equilibrium is valid in most of the star, apart for a thin shell near the stellar border. Towards the end of the evolution the dynamical time scale seems to reduce, and this is counterintuitive. In fact, we have associated the dynamical time scale with the neutrino time scale. This is not true towards the end of the evolution, since as the PNS becomes optically thin the neutrinos decouple from the matter and the diffusion approximation breaks down. At that point, the neutrino time scale drops, but the stellar dynamics is actually frozen.

3. Baryon gas assumption

In this paper we have not considered the formation of any kind of crust or envelope, that is, the EOS baryon part is

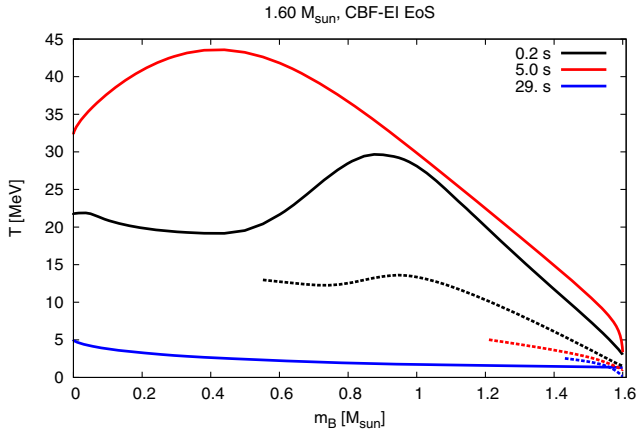

FIG. 14. Stellar temperature (solid lines) and critical temperature (dashed lines) for the formation of alpha particles at different times, for a PNS with the CBF-EI EOS and 1.60 $M_\odot$ baryon mass. When the baryon density reaches the nuclei density, 0.155 fm^{-3}, alpha particles could not form and we do not plot the critical temperature anymore.

made by an interacting gas of protons and neutrons. However, at low temperature and baryon density, the matter is not constituted by a gas of baryons only. The alpha particles (i.e., Helium nuclei) are the first species that appears decreasing the temperature and the density. The critical temperature at which alpha particles begin to form, that is, the lowest temperature at which protons and neutrons are present alone as an interacting gas, depends on the baryon density and the proton fraction. Equation (2.31) of [19] is an estimate of this critical temperature,

$$T_c(Y_p) = 87.76\left(\frac{K_s}{375\ \text{MeV}}\right)^{1/2}\left(\frac{0.155\ \text{fm}^{-3}}{n_s}\right)^{1/3} Y_p(1-Y_p)\ \text{MeV}, \tag{B9}$$

where n_s and K_s are the saturation density and the incompressibility parameter at saturation density of symmetric nuclear matter. Equation (B9) is valid for $n_B < n_s$, otherwise no alpha particles may form. In Fig. 14 we report the profiles of the critical temperature and the PNS temperature for different snapshots of a PNS with the CBF-EI EOS and with $M_B = 1.60\ M_\odot$; the results for the other EOSs and baryon masses are similar. As expected, the assumption of a proton-neutron interacting gas is valid at the beginning of the simulation and loses accuracy towards the end of the evolution, when it is not valid only in the outermost layers.

APPENDIX C: PNS QUASINORMAL MODES

In Tables III–XI we report the QNM frequencies and damping times for the models considered in this paper.

TABLE III. QNMs for a $M_B = 1.25\ M_\odot$ star evolved with the GM3 EOS. The column content, from left to right, is time of the snapshot (in s), frequency (in Hz) and damping time (in s) of the g_1-, f-, and p_1-modes, stellar gravitational mass (in $M_\odot$), and stellar radius (in km). The g_1-mode quantities are not shown when $\tau_{g_1} \gtrsim 10^7$ s.

t	ν_{g_1}	τ_{g_1}	ν_f	τ_f	ν_{p_1}	τ_{p_1}	M	R
0.2	784.1	4.01	955.3	2.49	1712	1.57	1.2064	22.444
0.3	776.6	5.91	928.2	2.18	1619	1.59	1.2051	23.530
0.4	768.0	11.5	925.7	1.75	1623	1.56	1.2036	23.320
0.5	752.9	25.9	940.5	1.48	1653	1.55	1.2021	22.917
0.6	734.4	58.2	965.2	1.31	1696	1.57	1.2006	22.430
0.7	715.1	123	995.0	1.17	1752	1.62	1.1992	21.894
0.8	695.8	247	1027	1.05	1817	1.71	1.1977	21.349
0.9	676.7	472	1058	0.952	1890	1.83	1.1962	20.812
1.0	658.2	873	1090	0.869	1976	1.98	1.1948	20.272
2.0	504.3	1.5×10^5	1300	0.534	3386	3.96	1.1828	15.893
4.0	326.8	2.8×10^5	1412	0.446	4593	5.96	1.1697	13.502
5.0	⋯	⋯	1433	0.434	4756	6.46	1.1660	13.215
10.0	⋯	⋯	1468	0.415	5017	6.77	1.1562	12.778
15.0	⋯	⋯	1475	0.413	5074	6.66	1.1520	12.659
20.0	⋯	⋯	1473	0.415	5091	6.88	1.1502	12.600

TABLE IV. As Table III, for a $M_B = 1.25\ M_\odot$ star with the CBF-EI EOS.

t	ν_{g_1}	τ_{g_1}	ν_f	τ_f	ν_{p_1}	τ_{p_1}	M	R
0.2	756.2	3.13	1036	4.41	1625	1.36	1.2118	23.807
0.3	753.2	3.35	1001	4.94	1546	1.38	1.2102	24.808
0.4	767.0	3.47	976.8	4.45	1549	1.34	1.2085	24.628
0.5	783.5	3.82	959.2	3.53	1572	1.30	1.2068	24.238
0.6	796.5	4.88	950.3	2.60	1604	1.27	1.2052	23.765
0.7	800.8	7.85	952.9	1.93	1643	1.25	1.2035	23.251
0.8	795.4	15.4	967.7	1.55	1686	1.25	1.2019	22.723
0.9	782.6	32.2	990.7	1.33	1732	1.26	1.2004	22.200
1.0	766.1	66.4	1019	1.18	1783	1.28	1.1988	21.679
2.0	568.0	2.5×10^4	1296	0.556	2542	2.32	1.1856	17.255
4.0	377.7	3.7×10^5	1512	0.385	4206	6.46	1.1695	13.684
5.0	⋯	⋯	1553	0.365	4643	7.75	1.1647	13.113
10.0	⋯	⋯	1635	0.330	5355	8.57	1.1535	12.240
15.0	⋯	⋯	1659	0.321	5507	8.04	1.1499	12.012
20.0	⋯	⋯	1664	0.319	5568	8.00	1.1492	11.903

TABLE V. As Table III, for a $M_B = 1.25\ M_\odot$ star with the LS-bulk EOS.

t	ν_{g_1}	τ_{g_1}	ν_f	τ_f	ν_{p_1}	τ_{p_1}	M	R
0.2	870.3	8.57	1047	1.21	1982	1.23	1.2020	19.925
0.3	839.0	22.0	1045	1.12	1888	1.27	1.2006	20.780
0.4	805.6	62.2	1068	1.01	1907	1.27	1.1992	20.506
0.5	772.9	161	1102	0.911	1961	1.30	1.1976	20.047
0.6	742.2	380	1139	0.821	2035	1.37	1.1961	19.533
0.7	713.6	829	1176	0.743	2125	1.46	1.1946	19.003
0.8	686.9	1.7×10^3	1213	0.676	2231	1.59	1.1931	18.467
0.9	662.0	3.4×10^3	1248	0.622	2353	1.74	1.1917	17.948
1.0	638.7	6.5×10^3	1279	0.579	2490	1.92	1.1903	17.446
2.0	473.5	5.9×10^6	1457	0.415	4027	3.22	1.1789	13.939
4.0	321.8	3.3×10^5	1538	0.372	4864	4.89	1.1673	12.557
5.0	278.9	5.9×10^5	1552	0.366	5010	5.28	1.1638	12.378
10.0	⋯	⋯	1572	0.359	5267	6.01	1.1540	12.091
15.0	⋯	⋯	1575	0.359	5328	6.15	1.1493	12.025
20.0	⋯	⋯	1575	0.360	5352	6.22	1.1465	11.986

TABLE VI. As Table III, for a $M_B = 1.40\ M_\odot$ star with the GM3 EOS.

t	ν_{g_1}	τ_{g_1}	ν_f	τ_f	ν_{p_1}	τ_{p_1}	M	R
0.2	695.5	3.28	954.3	4.83	1495	1.36	1.3553	25.961
0.3	712.6	3.38	924.5	4.62	1469	1.35	1.3536	26.289
0.4	734.6	3.67	904.4	3.61	1494	1.29	1.3518	25.782
0.5	751.3	4.78	895.6	2.54	1530	1.25	1.3500	25.174
0.6	757.2	8.21	901.1	1.83	1572	1.22	1.3482	24.560
0.7	752.5	17.2	919.9	1.46	1619	1.21	1.3464	23.937
0.8	741.5	37.5	947.4	1.24	1672	1.22	1.3447	23.312
0.9	727.4	78.7	979.1	1.09	1730	1.25	1.3429	22.704
1.0	712.1	156	1012	0.972	1793	1.29	1.3412	22.119
2.0	567.7	3.1×10^4	1284	0.484	2938	2.57	1.3260	17.122
4.0	387.1	4.6×10^6	1447	0.372	4461	4.15	1.3084	13.827
5.0	⋯	⋯	1476	0.357	4678	4.64	1.3033	13.450
10.0	⋯	⋯	1531	0.335	5050	5.14	1.2893	12.872
15.0	⋯	⋯	1545	0.330	5142	4.98	1.2827	12.725
20.0	⋯	⋯	1548	0.330	5175	4.95	1.2791	12.661

TABLE VII. As Table III, for a $M_B = 1.40\ M_\odot$ star with the CBF-EI EOS.

t	ν_{g_1}	τ_{g_1}	ν_f	τ_f	ν_{p_1}	τ_{p_1}	M	R
0.2	652.7	3.67	1029	6.68	1436	1.31	1.3613	27.434
0.3	665.1	3.60	1004	7.48	1410	1.31	1.3591	27.740
0.4	688.6	3.39	984.5	7.13	1430	1.26	1.3570	27.266
0.5	715.0	3.20	966.5	6.27	1462	1.21	1.3550	26.671
0.6	741.6	3.12	950.6	5.11	1498	1.16	1.3529	26.044
0.7	766.0	3.25	937.7	3.84	1536	1.12	1.3510	25.421
0.8	785.3	3.89	931.2	2.70	1578	1.09	1.3490	24.805
0.9	795.7	5.84	934.4	1.91	1621	1.07	1.3471	24.204
1.0	795.4	11.0	948.7	1.48	1666	1.06	1.3453	23.622
2.0	633.8	5.4×10^3	1239	0.556	2308	1.50	1.3290	18.681
4.0	381.0	3.7×10^5	1516	0.337	4010	4.28	1.3079	14.254
5.0	⋯	⋯	1568	0.315	4539	5.48	1.3013	13.520
10.0	⋯	⋯	1670	0.280	5459	7.33	1.2844	12.420
15.0	⋯	⋯	1703	0.270	5674	6.92	1.2778	12.146
20.0	⋯	⋯	1717	0.266	5761	6.69	1.2752	12.018

TABLE VIII. As Table III, for a $M_B = 1.40\ M_\odot$ star with the LS-bulk EOS.

t	ν_{g_1}	τ_{g_1}	ν_f	τ_f	ν_{p_1}	τ_{p_1}	M	R
0.2	821.7	2.70	1017	2.61	1739	1.00	1.3505	22.909
0.3	832.1	3.58	990.7	2.07	1708	0.993	1.3488	23.135
0.4	834.6	6.95	988.7	1.46	1739	0.958	1.3470	22.658
0.5	821.9	18.2	1010	1.16	1786	0.939	1.3451	22.081
0.6	800.7	49.2	1045	0.986	1846	0.938	1.3433	21.461
0.7	776.9	122	1086	0.862	1916	0.957	1.3415	20.833
0.8	752.7	278	1128	0.761	1996	0.996	1.3396	20.219
0.9	729.1	595	1171	0.677	2087	1.05	1.3379	19.615
1.0	706.3	1.2×10^3	1213	0.608	2190	1.13	1.3361	19.035
2.0	533.6	2.5×10^5	1472	0.359	3688	2.10	1.3214	14.668
4.0	⋯	⋯	1590	0.305	4757	3.42	1.3058	12.757
5.0	⋯	⋯	1610	0.298	4946	3.76	1.3012	12.532
10.0	⋯	⋯	1644	0.288	5299	4.41	1.2877	12.165
15.0	⋯	⋯	1650	0.288	5394	4.58	1.2807	12.082
20.0	⋯	⋯	1650	0.289	5431	4.64	1.2764	12.042

TABLE IX. As Table III, for a $M_B = 1.60\ M_\odot$ star with the GM3 EOS.

t	ν_{g_1}	τ_{g_1}	ν_f	τ_f	ν_{p_1}	τ_{p_1}	M	R
0.2	548.5	4.72	946.8	10.6	1232	1.41	1.5571	32.104
0.3	587.0	4.05	930.4	9.24	1276	1.32	1.5546	30.898
0.4	626.4	3.53	915.4	7.84	1329	1.22	1.5522	29.722
0.5	664.1	3.18	901.1	6.38	1381	1.14	1.5498	28.653
0.6	699.0	3.04	889.0	4.82	1433	1.07	1.5475	27.675
0.7	728.6	3.24	881.2	3.35	1484	1.02	1.5453	26.797
0.8	749.6	4.27	881.7	2.22	1535	0.983	1.5431	25.993
0.9	758.7	7.45	894.3	1.57	1586	0.958	1.5410	25.236
1.0	757.3	15.6	917.9	1.25	1640	0.946	1.5388	24.525
2.0	636.9	5.4×10^3	1239	0.464	2481	1.46	1.5195	18.838
4.0	458.1	6.7×10^5	1484	0.305	4246	2.61	1.4949	14.259
5.0	397.8	10^6	1526	0.289	4531	3.03	1.4877	13.735
10.0	⋯	⋯	1611	0.263	5050	3.69	1.4675	12.955
15.0	⋯	⋯	1636	0.256	5210	3.62	1.4572	12.750
20.0	⋯	⋯	1646	0.254	5261	3.51	1.4509	12.665

TABLE X. As Table III, for a $M_B = 1.60\ M_\odot$ star with the CBF-EI EOS.

t	ν_{g_1}	τ_{g_1}	ν_f	τ_f	ν_{p_1}	τ_{p_1}	M	R
0.2	522.7	7.45	995.1	20.4	1197	1.41	1.5637	33.618
0.3	549.3	5.01	986.9	15.3	1231	1.36	1.5606	32.492
0.4	581.2	4.17	978.8	12.3	1273	1.29	1.5577	31.376
0.5	614.4	3.62	969.0	10.4	1318	1.21	1.5551	30.341
0.6	647.5	3.21	957.7	8.95	1362	1.14	1.5525	29.389
0.7	680.3	2.90	945.4	7.56	1408	1.08	1.5500	28.496
0.8	711.9	2.69	933.3	6.14	1453	1.02	1.5476	27.677
0.9	741.4	2.62	922.2	4.67	1497	0.978	1.5452	26.910
1.0	767.2	2.80	914.3	3.28	1542	0.941	1.5430	26.187
1.1	786.1	3.58	913.0	2.20	1588	0.911	1.5407	25.510
1.2	794.6	5.98	921.9	1.55	1634	0.889	1.5386	24.860
1.3	792.6	12.2	941.4	1.22	1682	0.874	1.5364	24.234
1.4	783.8	26.1	967.9	1.04	1732	0.867	1.5343	23.633
1.8	725.5	365.	1095	0.691	1957	0.910	1.5263	21.458
1.9	709.4	648.	1127	0.635	2022	0.939	1.5244	20.962
2.0	693.2	1.1×10^3	1158	0.586	2090	0.975	1.5226	20.486
4.0	453.8	5.5×10^5	1522	0.291	3758	2.55	1.4944	14.944
5.0	⋯	⋯	1590	0.267	4348	3.37	1.4853	14.006
10.0	⋯	⋯	1714	0.233	5492	5.69	1.4600	12.639
15.0	⋯	⋯	1755	0.224	5801	5.88	1.4485	12.295
20.0	⋯	⋯	1776	0.220	5926	5.64	1.4425	12.143

TABLE XI. As Table III, for a $M_B = 1.60\ M_\odot$ star with the LS-bulk EOS.

t	ν_{g_1}	τ_{g_1}	ν_f	τ_f	ν_{p_1}	τ_{p_1}	M	R
0.2	662.9	3.07	1020	6.83	1440	0.997	1.5519	28.240
0.3	709.0	2.72	997.3	5.89	1494	0.919	1.5495	27.040
0.4	753.6	2.52	976.8	4.56	1555	0.846	1.5471	26.001
0.5	792.9	2.64	962.0	3.06	1618	0.787	1.5448	25.029
0.6	819.9	3.71	959.7	1.86	1680	0.745	1.5424	24.138
0.7	827.0	8.06	977.4	1.25	1743	0.717	1.5401	23.325
0.8	818.3	21.6	1012	0.988	1809	0.701	1.5379	22.547
0.9	802.1	55.8	1055	0.838	1879	0.699	1.5356	21.818
1.0	782.9	132	1102	0.728	1956	0.708	1.5334	21.124
2.0	606.4	5.3×10^4	1473	0.315	3237	1.24	1.5140	15.752
4.0	426.3	1.3×10^5	1657	0.245	4586	2.17	1.4924	12.975
5.0	374.9	9.2×10^6	1687	0.237	4825	2.44	1.4860	12.678
10.0	⋯	⋯	1742	0.225	5304	3.03	1.4670	12.201
15.0	⋯	⋯	1755	0.223	5452	3.19	1.4568	12.081
20.0	⋯	⋯	1757	0.224	5510	3.25	1.4500	12.032

[1] A. Burrows and J. M. Lattimer, Astrophys. J. **307**, 178 (1986).
[2] W. Keil and H.-T. Janka, Astron. Astrophys. **296**, 145 (1995).
[3] J. A. Pons, S. Reddy, M. Prakash, J. M. Lattimer, and J. A. Miralles, Astrophys. J. **513**, 780 (1999).
[4] K. Hirata *et al.*, Phys. Rev. Lett. **58**, 1490 (1987).
[5] R. M. Bionta *et al.*, Phys. Rev. Lett. **58**, 1494 (1987).
[6] H. T. Janka, T. Melson, and A. Summa, Annu. Rev. Nucl. Part. Sci. **66**, 341 (2016).
[7] L. Hüdepohl, B. Müller, H.-T. Janka, A. Marek, and G. G. Raffelt, Phys. Rev. Lett. **104**, 251101 (2010).
[8] T. Fischer, S. C. Whitehouse, A. Mezzacappa, F.-K. Thielemann, and M. Liebendörfer, Astron. Astrophys. **517**, A80 (2010).
[9] A. Burrows, Astrophys. J. **334**, 891 (1988).
[10] L. F. Roberts, G. Shen, V. Cirigliano, J. A. Pons, S. Reddy, and S. E. Woosley, Phys. Rev. Lett. **108**, 061103 (2012).
[11] T. Takiwaki, K. Kotake, and Y. Suwa, Astrophys. J. **786**, 83 (2014).
[12] T. Melson, H.-T. Janka, and A. Marek, Astrophys. J. Lett. **801**, L24 (2015).
[13] B. Müller, Mon. Not. R. Astron. Soc. **453**, 287 (2015).
[14] L. F. Roberts, Astrophys. J. **755**, 126 (2012).
[15] V. Ferrari, G. Miniutti, and J. A. Pons, Mon. Not. R. Astron. Soc. **342**, 629 (2003).
[16] V. Ferrari, L. Gualtieri, J. Pons, and A. Stavridis, Mon. Not. R. Astron. Soc. **350**, 763 (2004).
[17] G. F. Burgio, V. Ferrari, L. Gualtieri, and H.-J. Schulze, Phys. Rev. D **84**, 044017 (2011).
[18] H. Sotani and T. Takiwaki, Phys. Rev. D **94**, 044043 (2016).
[19] J. M. Lattimer and F. D. Swesty, Nucl. Phys. **A535**, 331 (1991).
[20] O. Benhar and A. Lovato, arXiv:1706.00760.
[21] A. Lovato, O. Benhar, and G. Camelio (unpublished).
[22] N. K. Glendenning, Astrophys. J. **293**, 470 (1985).
[23] N. K. Glendenning and S. A. Moszkowski, Phys. Rev. Lett. **67**, 2414 (1991).
[24] F. D. Swesty, J. Comput. Phys. **127**, 118 (1996).
[25] I. Bombaci and U. Lombardo, Phys. Rev. C **44**, 1892 (1991).
[26] G. F. Burgio and H.-J. Schulze, Astron. Astrophys. **518**, A17 (2010).
[27] S. Balberg and A. Gal, Nucl. Phys. **A625**, 435 (1997).
[28] C. Ducoin, J. Margueron, C. Providência, and I. Vidaña, Phys. Rev. C **83**, 045810 (2011).
[29] N. Alam, B. K. Agrawal, M. Fortin, H. Pais, C. Providência, A. R. Raduta, and A. Sulaksono, Phys. Rev. C **94**, 052801 (2016).
[30] P. P. Eggleton, J. Faulkner, and B. P. Flannery, Astron. Astrophys. **23**, 325 (1973).
[31] S. M. Johns, P. J. Ellis, and J. M. Lattimer, Astrophys. J. **473**, 1020 (1996).
[32] S. Reddy, M. Prakash, and J. M. Lattimer, Phys. Rev. D **58**, 013009 (1998).
[33] T. Fischer, Astron. Astrophys. **593**, A103 (2016).
[34] R. W. Lindquist, Ann. Phys. (N.Y.) **37**, 487 (1966).
[35] J. R. Wilson and R. W. Mayle, in *NATO Advanced Science Institutes (ASI) Series B*, Vol. 216, edited by W. Greiner and H. Stöcker (Plenum, New York, 1989), p. 731.
[36] W. H. Press, S. A. Teukolsky, W. T. Vetterling, and B. P. Flannery, *Numerical Recipes in Fortran 77*, 2nd ed. (Cambridge University Press, Cambridge, England, 1992).
[37] C. D. Levermore and G. C. Pomraning, Astrophys. J. **248**, 321 (1981).
[38] G. Camelio, Ph.D. Thesis, Università di Roma "Sapienza", Dipartimento di Fisica (2017).
[39] W. Kunkel, B. Madore, I. Shelton, O. Duhalde, F. M. Bateson, A. Jones, B. Moreno, S. Walker, G. Garradd, B. Warner, and J. Menzies, IAU Circular No. 4316 (1987).
[40] J. M. Lattimer and A. Yahil, Astrophys. J. **340**, 426 (1989).
[41] M. Ikeda *et al.*, Astrophys. J. **669**, 519 (2007).
[42] J. Hosaka *et al.*, Phys. Rev. D **73**, 112001 (2006).
[43] K. S. Thorne and A. Campolattaro, Astrophys. J. **149**, 591 (1967).
[44] S. Chandrasekhar and V. Ferrari, Proc. R. Soc. A **432**, 247 (1991).
[45] S. Detweiler and L. Lindblom, Astrophys. J. **292**, 12 (1985).
[46] H. Andresen, B. Müller, E. Müller, and H.-T. Janka, Mon. Not. R. Astron. Soc. **468**, 2032 (2017).
[47] T. Kuroda, K. Kotake, and T. Takiwaki, Astrophys. J. **829**, L14 (2016).
[48] K. Kotake, C.R. Phys. **14**, 318 (2013).
[49] R. F. Christy, Annu. Rev. Astron. Astrophys. **4**, 353 (1966).
[50] A. Lovato, C. Losa, and O. Benhar, Nucl. Phys. **A901**, 22 (2013).
[51] A. Lovato, O. Benhar, S. Gandolfi, and C. Losa, Phys. Rev. C **89**, 025804 (2014).
[52] L. F. Roberts and S. Reddy, Phys. Rev. C **95**, 045807 (2017).